

Star-formation rates from young-star counts and the structure of the ISM across the NGC 346/N66 complex in the SMC*

S. Hony^{1†}, D. A. Gouliermis^{1,2}, F. Galliano³, M. Galametz⁴, D. Cormier¹, C.-H. R. Chen⁵, S. Dib^{6,7}, A. Hughes^{8,9,2}, R. S. Klessen^{1,10,11}, J. Roman-Duval¹², L. Smith¹³, J.-P. Bernard^{8,9}, C. Bot¹⁴, L. Carlson¹⁵, K. Gordon^{12,16}, R. Indebetouw^{15,17}, V. Lebouteiller³, M.-Y. Lee³, S. C. Madden³, M. Meixner^{12,18}, J. Oliveira¹⁹, M. Rubio²⁰, M. Sauvage³, R. Wu²¹

¹Universität Heidelberg, Zentrum für Astronomie, Institut für Theoretische Astrophysik, Albert-Ueberle-Str. 2, 69120 Heidelberg, Germany ²Max Planck Institute for Astronomy, Königstuhl 17, 69117 Heidelberg, Germany ³Laboratoire AIM, CEA/IRFU/Service d'Astrophysique, Université Paris Diderot, Bat. 709, 91191 Gif-sur-Yvette, France ⁴European Southern Observatory, Karl-Schwarzschild-Str. 2, 85748 Garching-bei-München, Germany ⁵Max-Planck-Institut für Radioastronomie, Auf dem Hügel 69, 53121 Bonn, Germany ⁶Niels Bohr International Academy, Niels Bohr Institute, Blegdamsvej 17, 2100, Copenhagen, Denmark ⁷Centre for Star and Planet Formation, University of Copenhagen, Øster Voldgade 5-7, 1350, Copenhagen, Denmark ⁸CNRS, IRAP, 9 Av. Colonel Roche, BP 44346, 31028 Toulouse Cedex 4, France ⁹Université de Toulouse, UPS-OMP, IRAP, 31028 Toulouse Cedex 4, France ¹⁰Department of Astronomy and Astrophysics, University of California, 1156 High Street, Santa Cruz, CA 95064, USA ¹¹Kavli Institute for Particle Astrophysics and Cosmology, Stanford University, SLAC National Accelerator Laboratory, Menlo Park, CA 94025, USA ¹²Space Telescope Science Institute, 3700 San Martin Drive, Baltimore, MD 21218, USA ¹³Space Telescope Science Institute and European Space Agency, 3700 San Martin Drive, Baltimore, MD 21218, USA ¹⁴Observatoire astronomique de Strasbourg, Université de Strasbourg, CNRS, UMR 7550, 11 rue de l'Université, 67000 Strasbourg, France ¹⁵Department of Astronomy, University of Virginia, PO Box 3818, Charlottesville, VA 22903, USA ¹⁶Sterrenkundig Observatorium, Universiteit Gent, Gent, Belgium ¹⁷National Radio Astronomical Observatory, Charlottesville, VA 22904, USA ¹⁸The Johns Hopkins University, Department of Physics and Astronomy, 366 Bloomberg Center, 3400 N. Charles Street, Baltimore, MD 21218, USA ¹⁹School of Physical & Geographical Sciences, Lennard-Jones Laboratories, Keele University, Staffordshire ST5 5BG, UK ²⁰Departamento de Astronomia, Universidad de Chile, Casilla 36-D, Santiago, Chile ²¹Department of Astronomy, Graduate School of Science, The University of Tokyo, Bunkyo-ku, Tokyo 113-0033, Japan

Accepted 2015 January 15. Received 2015 January 14; in original form 2014 October 30

ABSTRACT

The rate at which interstellar gas is converted into stars, and its dependence on environment, is one of the pillars on which our understanding of the visible Universe is build. We present a comparison of the surface density of young stars (Σ_*) and dust surface density (Σ_{dust}) across NGC 346 (N66) in 115 independent pixels of $6 \times 6 \text{ pc}^2$. We find a correlation between Σ_* and Σ_{dust} with a considerable scatter. A power law fit to the data yields a steep relation with an exponent of 2.6 ± 0.2 . We convert Σ_{dust} to gas surface density (Σ_{gas}) and Σ_* to star formation rate (SFR) surface densities (Σ_{SFR}), using simple assumptions for the gas-to-dust mass ratio and the duration of star formation. The derived total SFR ($4 \pm 1 \cdot 10^{-3} \text{ M}_{\odot} \text{ yr}^{-1}$) is consistent with SFR estimated from the $\text{H}\alpha$ emission integrated over the $\text{H}\alpha$ nebula. On small scales the Σ_{SFR} derived using $\text{H}\alpha$ systematically underestimates the count-based Σ_{SFR} , by up to a factor of 10. This is due to ionizing photons escaping the area, where the stars are counted. We find that individual 36 pc^2 pixels fall systematically above integrated disc-galaxies in the Schmidt-Kennicutt diagram by on average a factor of ~ 7 . The NGC 346 average SFR over a larger area (90 pc radius) lies closer to the relation but remains high by a factor of ~ 3 . The fraction of the total mass (gas plus young stars) locked in young stars is systematically high (~ 10 per cent) within the central 15 pc and systematically lower outside (2 per cent), which we interpret as variations in star formation efficiency. The inner 15 pc is dominated by young stars belonging to a centrally condensed cluster, while the outer parts are dominated by a dispersed population. Therefore, the observed trend could reflect a change of star formation efficiency between clustered and non-clustered star-formation.

Key words: ISM: individual: NGC 346 – ISM: Structure – stars: pre-main-sequence – galaxies: Magellanic Clouds

* based on observations obtained with *HST*, *Spitzer*, *Herschel* and *APEX*.

† E-mail: sacha.hony@free.fr

1 INTRODUCTION

It is generally accepted that the local star-formation rate (SFR) scales with the local gas density of the interstellar medium (ISM). This wisdom is captured in the Schmidt-Kennicutt relation (SK-relation, see for a review Kennicutt & Evans 2012) which connects the observed gas-surface density (Σ_{gas}) along various sight-lines with the observed surface density of SFR (Σ_{SFR}). Even though there are multiple incarnations of the Schmidt-Kennicutt diagram, depending on which tracers are used to measure both Σ_{gas} and Σ_{SFR} , and whether to consider only the dense (molecular) gas or include the atomic phase, the emerging picture is clear: the higher the ISM column density, the higher the star-formation rate. A key feature of the SK-relation is its power law behaviour over a large dynamic range of gas column-densities and star-formation rates. The slope of the relation depends on whether one measures only the dense gas (exponent ~ 1) or also the atomic gas (exponent ~ 1.4).

The physical interpretation of this interdependence, i.e. how to derive the efficiency with which interstellar gas is converted into stars, is much less self-evident, especially on small spatial scales (< 1 kpc). This is due to the following: *i*) The ‘star-formation rate’ measures stars that have already formed, while the gas column density relates to (the capacity for) future star formation. On small scales, with low numbers of stars, one can no longer expect to measure a time-averaged efficiency as is the case when averaging over a large number of star forming sites. *ii*) Dynamical simulations (e.g. Kiseleva et al. 1998) and observations (e.g. Goodman 2004) show that young stars may be displaced, by several pc per Myr, from the location where they were born, and thus removed from the reservoir of gas from which they formed *iii*) The large scale averages include non-star-forming parts of the ISM and the relative proportion of this ‘inactive’ gas will change when zooming in on smaller scales. *iv*) Many of the used SFR-tracers (e.g. $\text{H}\alpha$ or far-ultraviolet (FUV) emission) are sensitive only to high-mass stars, which represent only a fraction of the stellar mass assembled in the star-formation event and to derive the total SFR one needs to extrapolate the mass-function to lower masses. Since the high-mass slope of the initial mass function (IMF) is very steep – very few of the formed stars are high-mass – the corrections are large and sensitive to the assumed shape of the IMF. Some or all of these effects are probably the reason why the studies of star formation rates in nearby individual molecular clouds (Evans et al. 2009; Wu et al. 2010; Heiderman et al. 2010; Gutermuth et al. 2011) find very different star formation rates at a given gas column density compared to global averages.

The aim of this paper is to circumvent some of these complications by studying the correlation between newly formed stars and the gas reservoir (Σ_{SFR} , and Σ_{gas}) in many small beams (~ 6 pc) which cover an entire star forming complex. We investigate, thus, the small scale relation between young stars and gas reservoir while covering a larger region. We use the most direct way of determining Σ_{SFR} , i.e. by counting the newly assembled stars. At the same time we employ the ‘dust method’ to determine the ISM column density, i.e. using the infrared (IR) to submillimetre (submm) dust continuum emission to derive dust surface densities. This method has the advantage of not being sensitive to the state of the gas (ionized, neutral or molecular) as long as dust and gas are well mixed. This insensitivity is important because we will use a catalogue of low- and intermediate-mass pre-main sequence (PMS) stars plus upper-main sequence (UMS) stars, i.e. O and B type stars, as the basis for our star counts. Due to the evolutionary stage of the PMS stars – a few Myr after the onset of star formation – the parental molecular

complex may have been subject to significant photo-dissociation and using a molecular gas tracer (such as CO) may lead to an incomplete view of the total gas surface densities.

The object of choice is the star-forming complex related to NGC 346, also often referred to as N66. NGC 346 is the most prominent star-formation region in the Small Magellanic Cloud (SMC). In order to assess the Σ_{SFR} , an unbiased census of the young stellar population is required. This is available for NGC 346 thanks to *HST* observations (Nota et al. 2006; Gouliermis et al. 2006, see Sect. 3.1). We have access to sensitive IR to submm photometry from *Spitzer* (PI Gordon), *Herschel* (PI Meixner) and *APEX/Laboca* (PI Hony) in order to derive reliable dust surface densities. The proximity (60 kpc) of the SMC in combination with the size of the star forming complex ($\sim 100 \times 100 \text{ pc}^2$) enables us to ‘zoom in’ (~ 6 pc linear scale) and study local variations at the angular resolution of the available submm observations.

Moreover, the entire complex encompasses a range of environments. In terms of the ISM, the region exhibits a wide range of surface brightness of hot dust ($24 \mu\text{m}$), polycyclic aromatic hydrocarbon (PAH; $8 \mu\text{m}$) and molecular gas ($\text{CO}(J=2-1)$, Rubio et al. 2000). In terms of the stellar content, there are zones which are cluster dominated as well as regions where the young stars are more dispersed (Gouliermis, Hony & Klessen 2014). This allows us to examine how the environment influences the relation between star formation and the available ISM reservoir. The main questions we address are:

- How well do young stars and the densest ISM track each other?
- Do star counts yield the same Σ_{SFR} as indirect tracers?
- Does the efficiency of star formation vary between clustered and more extended spatial distributions?
- What is the effect of averaging over different scales on the derived parameters in the position in the SK-diagram?

Additionally, we examine whether there may be an effect of the reduced metal abundance of the SMC (0.2 solar, Haser et al. 1998) on the star formation efficiency.

The paper is organised as follows. Previous work on deriving SFR from individual young sources is reviewed in Sect. 2. In Sect. 3 we present the catalogue of young stars and the IR to submm data-sets that we use for our analysis. We further describe the data treatment to derive independent surface density measurements in $20 \times 20 \text{ arcsec}^2$ ($6 \times 6 \text{ pc}^2$) beams (Sect. 3.4). Our methodology to obtain gas surface densities, using SED fitting, is described in Sect. 4.1 and 4.2. The SFR derived from our young star counts is compared to indirect SFR tracers in Sect. 4.3. In Sect. 5 we compare the derived Σ_{gas} and Σ_{SFR} . Possible biases that may affect the observed value of $\Sigma_{\text{SFR}}/\Sigma_{\text{gas}}$ are discussed in Sect. 6. We conclude in Sect. 7.

2 PREVIOUS WORK

Most of the work done on comparing ISM column densities and star-formation rates based on individual objects has concentrated on nearby (within one kpc from the sun) Milky Way star-forming sites (Evans et al. 2009; Lada, Lombardi & Alves 2010; Heiderman et al. 2010; Wu et al. 2010; Gutermuth et al. 2011). These studies have consistently shown that when one considers the immediate dense environment (on a few parsec scales) surrounding the newly formed stars, the derived SFR is higher than predicted

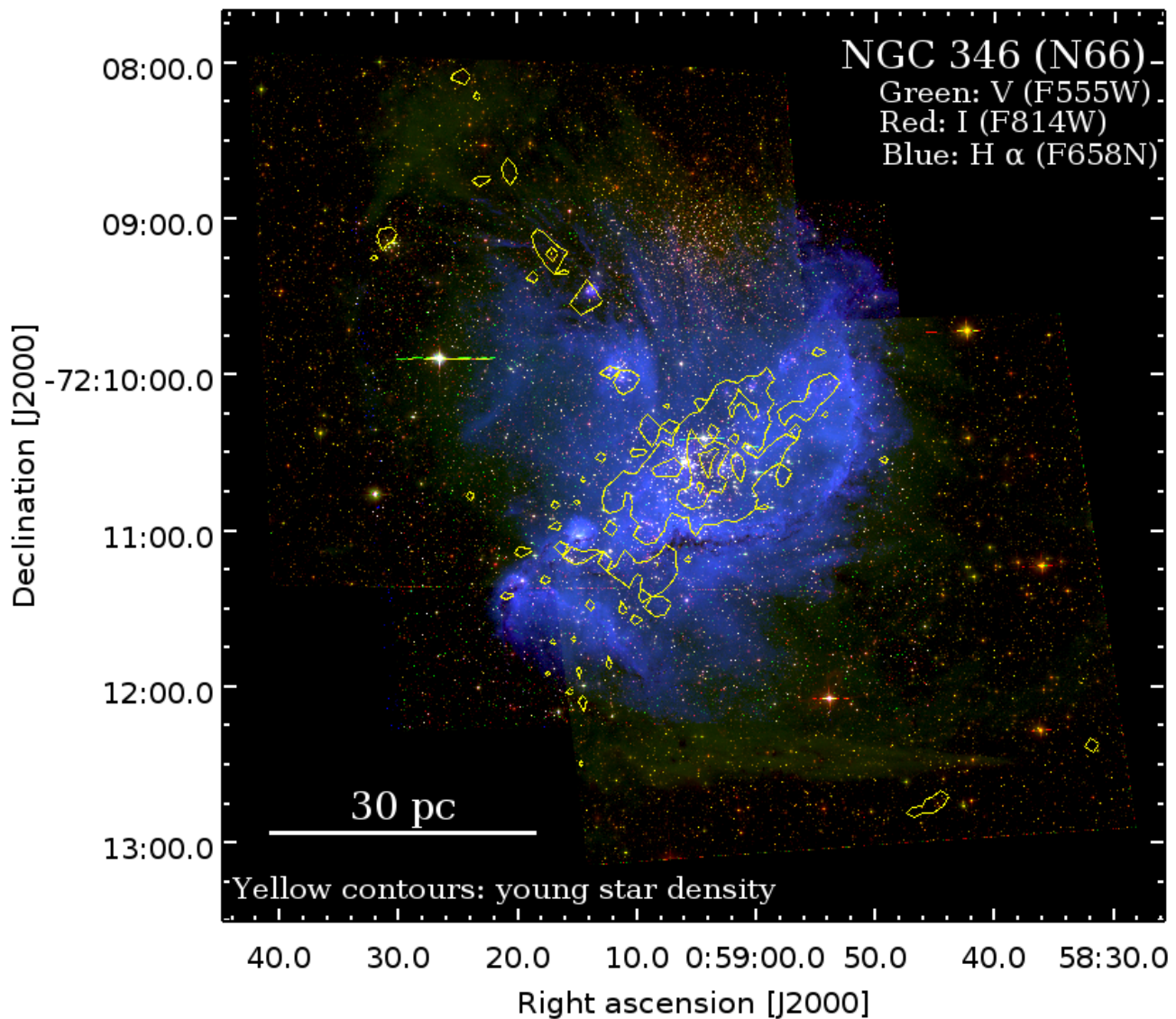


Figure 1. False colour composite image (green: optical, red: infrared, blue H α) of NGC 346 based on *HST* imaging (PI Nota, Nota et al. 2006). The contours of the, 2 arcsec resolution, density map (Σ_{\star}) of the young stars are shown in yellow. The contour levels correspond to 3, 10 and 20 stars pc^{-2} . The maximum value of Σ_{\star} is 45 stars pc^{-2} .

by the galaxy averaged SK-relation (by up to a factor of 54) for a given ISM column density.

Evans et al. (2009); Lada, Lombardi & Alves (2010) present the total star-formation rates based on young stellar object (YSO) candidates, identified from their mid-IR excess using *Spitzer* and compare those to molecular cloud masses derived using extinction maps for ~ 10 nearby molecular clouds. These studies show that there is a large variety of star formation efficiency (SFE) among those clouds. Lada, Lombardi & Alves (2010) show that some of the observed spread in SFE disappears when considering only the mass of gas above an extinction threshold of $A_K > 0.8$ mag. They interpret this as an indication for a density threshold below which star-formation does not occur. A similar conclusion is reached by Heiderman et al. (2010) who study the Σ_{SFR} versus Σ_{gas} within those clouds using YSOs. The typical spatial scale over which they compare these quantities is from a few tenths of a parsec to a few

parsec. Their data show a very sharp decrease in Σ_{SFR} below $\Sigma_{\text{gas}} \approx 10^2 \text{ M}_{\odot} \text{ pc}^{-2}$ which is interpreted as resulting from a density threshold for star-formation. Note, that such a threshold, if it exists, cannot be a *universal* threshold. There are several observations of specific regions whose gas surface densities exceed the threshold, with much less star formation than would be expected (e.g. Longmore et al. 2013; Rathborne et al. 2014). Moreover, the existence of a column density-threshold for star formation in a turbulent ISM is not supported by theoretical models (Clark & Glover 2014).

A different picture emerges from the analysis presented by Gutermuth et al. (2011). These authors present scatter diagrams of surface density of from YSOs versus Σ_{gas} (from extinction) for eight molecular clouds within 1 kpc from the sun. They find a steep power law correlation (with indices between 1.4 and 2.7, with an outlier at 3.8) with significant scatter and no indication for a density threshold. They argue that the data are consistent with a SFR which

Table 1. Values and symbols used throughout this paper.

Quantity	Symbol	Value	Comments/Refs
SMC distance	d_{SMC}	60 ± 3 kpc	Harries, Hilditch & Howarth (2003)
Detected young stars	N_{star}	5150	Gouliermis et al. (2006), see Sect. 3.1
Total young stellar mass	M_{tot}	$2.2 \cdot 10^4 M_{\odot}$	Sabbi et al. (2008), see Sect. 3.1
Mass per catalogue source	M_{cat}^a	$4.3 M_{\odot}$	$= M_{\text{tot}} N_{\text{star}}^{-1}$, see Sect. 3.1
SF duration	Δt_{SFR}	$5 \cdot 10^6$ yr	Mokiem et al. (2006), see Sect. 3.1
Gas-to-dust mass ratio	r_{gd}	1250	Sect. 4.2
Derived Quantity			
Young star surface density	Σ_{\star}		from star catalogue
Stellar mass surf. dens.	$\Sigma_{M_{\star}}$		$= \Sigma_{\star} \cdot M_{\text{cat}}$
SFR surf. dens.	Σ_{SFR}		$= \Sigma_{M_{\star}} \Delta t_{\text{SFR}}^{-1}$
Dust surf. dens.	Σ_{dust}		from SED fitting
Gas surf. dens.	Σ_{gas}		$= \Sigma_{\text{dust}} \cdot r_{\text{gd}}$
Stellar mass fraction	$\text{frac}_{M_{\star}}$		$= \Sigma_{M_{\star}} (\Sigma_{M_{\star}} + \Sigma_{\text{gas}})^{-1}$

^aThis mass is *not* the mean mass of the *HST* detected sources but the mass each source represents after correcting for completeness. The mean mass of the young stars in the *HST* catalogue is $\sim 2 M_{\odot}$.

is proportional to Σ_{gas}^2 . Note that the different conclusion reached by the latter authors is based, in part, on the way the surface density of YSOs is calculated in the low surface-density regime as they use the *n*th-nearest-neighbour centred on the detected YSOs. We further note that, given the steep dependence on Σ_{SFR} and the low number counts, distinguishing between a threshold and this power law is difficult and almost a matter of semantics.

The work by Gutermuth et al. (2011) is the Galactic study that can be compared most directly to the NGC 346 analysis we present here, because their Σ_{gas} maps cover several tens of parsecs around the molecular clouds and each cloud harbours a significant number (>100) of YSOs. Compared to the work we present here, these previous studies have the advantage of proximity and as a result, they are able to examine the star-formation within individual molecular clouds on spatial scales of <1 pc while the best angular resolution we can attain in the SMC in the ISM tracers is ~ 6 pc.

Recent *Spitzer* surveys of the Large and Small Magellanic Clouds (LMC and SMC) made it possible to use resolved massive YSOs to determine current SFRs outside of the Galaxy. Unlike the consistently higher SFRs of small-size clouds reported in the aforementioned Galactic studies, Chen et al. (2010) showed that current SFR determined from massive YSOs in individual giant molecular clouds in H II complexes in the LMC are distributed above and below the SK relation, depending on the evolutionary states of the giant molecular cloud. The scatter in SFR diminishes and follow the SK relation when properties are averaged over the entire H II complexes of 150–200 pc. This is in agreement with the findings of Kruijssen & Longmore (2014), who attribute the scatter on smaller scales to incomplete statistical sampling of independent star-forming regions. Furthermore, the commonly used SFR tracers such as H α and $24 \mu\text{m}$ luminosities would under-estimate the amount of star formation in regions not actively producing O-type stars, such as the LMC's largest molecular ridge and the Magellanic Bridge. They show that using H α or $24 \mu\text{m}$ as SFR tracers these points are outliers on the SK-relation while they follow the SK-relation when using SFR determined from YSO counts (Indebetouw et al. 2008; Chen et al. 2014).

The work presented here differs from these previous studies by the sources we use to trace the star formation (PMS+UMS stars versus YSOs) and the way we derive the ISM column den-

sities (dust emission versus extinction). This has the following (dis-)advantages:

- Rich stellar catalogue: *HST* has provided accurate photometry for more than 5 000 stellar sources covering the pre-main-sequence (Gouliermis et al. 2006).
- Measured mass function and age: ages and the mass function have been determined for the UMS+PMS stellar catalogue (Sabbi et al. 2008). This means we can rely on the observed mass function, which covers a significant (0.8–40 M_{\odot}) part of the entire mass range, and the observed duration of the star-formation event to derive the SFR. The YSOs studies assume a typical age and mass for a YSO, both of which are uncertain (e.g. Preibisch 2012), which could introduce a large *systematic* uncertainty.
- Large coverage: the IR and submm observations that we use to measure dust column densities are very sensitive and most cover the entire SMC (Sect. 3.2). As a result, we have access to an unbiased probe of the dust surface density out to large distances and low column densities. This is important to assess the behaviour of the SFR at low Σ_{gas} , where significant disagreement exists in the literature (see above).

However, since we are using stars that are no longer embedded, the sources in our catalogue are more evolved (<5 Myr, Sect. 3.1) than YSOs (<2 Myr) and have had more time to displace (or be displaced from) their parental gas reservoir. Moreover, since the whole region has to be more evolved for it to host so many PMS stars, the radiation from the hot, young stars has had more time to affect the surrounding medium.

3 OBSERVATIONS

3.1 Young stellar catalogue

Imaging with the Hubble Space Telescope (*HST*) of star-forming regions in the Magellanic Clouds has provided access to exceptionally rich samples of newly-born stars down to the sub-solar regime over large areas of the sky. Our catalogue of young stars in NGC 346, one of the largest star-forming complexes in the SMC, is among the richest Magellanic Clouds stellar ensembles ever collected with *HST*. Three pointings (with significant offsets), centred

on NGC 346 were observed with the Wide-Field Channel (WFC) of ACS covering an area of about $5 \times 5 \text{ arcmin}^2$ ($\sim 88 \times 88 \text{ pc}^2$). The images were obtained within the HST Program GO-10248 (PI Nota, Nota et al. 2006) in the filters F555W and F814W (equivalent to standard V and I bands). Detailed descriptions of the data reduction and photometry are given in Gouliermis et al. (2006). The photometry reveals more than 98 000 stars at various evolutionary stages, and its 50% completeness limit is $m_{555} \simeq 27$ (Gouliermis et al. 2006).

The sample of young stellar populations in NGC 346 consists of the low-mass pre-main-sequence (PMS) stars, which are identified from their faint-red positions on the colour–magnitude diagram (CMD). See Gouliermis (2012) for a review on low-mass PMS stars in the Magellanic Clouds. This sample is complemented by the UMS stars (selected with colours $m_{555} - m_{814} \leq 0.0$ and magnitudes $12 \sim m_{555} \lesssim 17$), including more than 30 early-type stars (see also Massey, Parker & Garmany 1989; Mokiem et al. 2006). The masses of the selected UMS stars are such that they would have evolved off the main sequence if they were older than the PMS population. Thus, the catalogue we use in this analysis contains 5 150 young (PMS and UMS) stars in the mass range between $\sim 0.5 M_{\odot}$ and $\sim 40 M_{\odot}$. The location of the young stars within the complex is indicated in Fig. 1 with yellow contours. This image shows the very prominent $H\alpha$ emission associated with the central cluster and the presence of several secondary clusters of young stars to the North which cause little $H\alpha$ emission.

It is hard to get accurate age and mass determinations of the individual PMS stars based on their position in the CMD (Jeffries 2012). An isochronal median age around $\sim 3 \text{ Myr}$ has been defined for the *ensemble* of PMS stars in NGC 346 on the basis of comparison with evolutionary models (Sabbi et al. 2008; Cignoni et al. 2011). Mokiem et al. (2006) have spectroscopically studied the high-mass stars towards NGC 346. They find ages between 0 and 5 Myr for the high-mass stars that belong to the star-formation complex. This age range is fully compatible with the position and spread of the low-mass PMS stars in the CMD. Since our objective is to measure the *average* SFR counting *all* stars that have formed during the star-formation event, we use 5 Myr as the star-formation duration (Δt_{SFR}). Thus, Δt_{SFR} refers to the duration of the event *not* to the ages of the individual stars. Therefore, this approach is conceptually different from the YSO-counting studies (e.g. Lada, Lombardi & Alves 2010; Heiderman et al. 2010) in which ages of the individual objects have been assumed.

We construct the entire mass function of the UMS+PMS catalogue by extrapolating the mass function for masses above $0.8 M_{\odot}$ derived by Sabbi et al. (2008, Fig 3 bottom panel) from the same observational material. Their mass function is completeness corrected for crowding and photometric sensitivity but not for interstellar extinction. Over the measured range the mass function has a slope of -1.43^1 . We extrapolate to lower masses using a Kroupa mass function with a slope of -0.3 between 0.08 and $0.5 M_{\odot}$ and a slope of 0.7 between 0.01 and $0.08 M_{\odot}$ (Kroupa 2001). The total stellar mass formed in the last 5 Myr, obtained by integrating this mass function and multiplying by the survey area ($88 \times 88 \text{ pc}^2$) equals $\sim 2.24 \cdot 10^4 M_{\odot}$. Since we have 5 150 stars in our catalogue, each source represents on average a mass of $4.3 M_{\odot}$ (M_{cat}). The

mass in directly detected stars ($M_{\star} > 0.8 M_{\odot}$) is $1.2 \cdot 10^4 M_{\odot}$, i.e. 50 per cent of the total. The main parameters used in our analysis are summarised in Tab. 1.

The total star formation rate, averaged over the last 5 Myr, of the complex calculated in this way is $4 \pm 1 \cdot 10^{-3} M_{\odot} \text{ yr}^{-1}$, where the uncertainty takes into account possible star formation outside of the field-of-view of *HST* (20 per cent) and the extrapolation of the observed mass function to lower masses (20 per cent) but not the systematic uncertainty due the assumed duration of the star formation event. This value is consistent with the results of Simon et al. (2007) who find a SFR $> 3.2 \cdot 10^{-3} M_{\odot} \text{ yr}^{-1}$ over the last 1 Myr using *Spitzer* identified YSO candidates.

For the rest of the analysis we assume that the mass function and the duration of star formation are invariant across the star forming complex. There are some indications of variations in the slope of the mass function in NGC 346 (Sabbi et al. 2008; Cignoni et al. 2011). The general trend is a steepening of the slope with increasing distance to the central cluster, i.e. a larger fraction of high-mass stars towards the central cluster, consistent with a certain degree of mass segregation in the cluster. However, such variations have little impact on our results which are based on star counts, while luminosity based SFR tracers (e.g. $H\alpha$) are very sensitive to the number of high-mass stars and thus the high-mass slope of the mass function. As an illustration of this invariance consider the standard Kroupa mass function (Kroupa 2001) with a high-mass power law slope of -1.3 . When we vary this slope between -1.0 and -2.0 – the observed range of slopes in NGC 346 (Sabbi et al. 2008) – the total mass per number of stars above $0.8 M_{\odot}$ (i.e. M_{cat}) varies by only ~ 20 per cent. For the same variations in slope the fraction of mass locked in the high-mass stars – those powering the $H\alpha$ emission ($M_{\star} > 8 M_{\odot}$) – varies by 1500 per cent!

3.2 Herschel and Spitzer data

We use the mid-IR to submm photometric maps that have been obtained with *Spitzer* (SAGE-SMC: Gordon et al. 2011) and *Herschel* (HERITAGE: Meixner et al. 2013). Within these two large programs the entire SMC has been observed at IRAC (3.6, 4.5, 5.8 and $8.0 \mu\text{m}$), MIPS (24, 70, and $160 \mu\text{m}$), PACS (100 and $160 \mu\text{m}$) and SPIRE (250, 350 and $500 \mu\text{m}$) wavelengths. The sensitivity of these data sets is such that for the environment of the prominent star forming region NGC 346 the photometric uncertainty is dominated by the absolute flux calibration (see also Sect. 3.4). An overview of NGC 346 in some key ISM tracers is shown in Fig. 2. In the following analysis we mainly use the IRAC, MIPS-24, MIPS-70, PACS-100, PACS-160 and SPIRE-250 data, because these sufficiently cover the spectral energy distribution (SED) to derive accurate dust surface densities at optimal angular resolution ($\sim 20 \text{ arcsec}$). The SPIRE 350 μm and 500 μm data have poorer angular resolution. The only exception is the dust masses derived within large circular apertures (Tab. 2) which uses the SPIRE-350 μm data to replace the *Laboca* because the latter is not observed over such a large area.

3.3 Laboca 870 μm imaging data

To constrain the emission by the coolest dust, we use *Laboca* data at $870 \mu\text{m}$, instead of the SPIRE 350 data. This data set allows us to obtain measurements at $\sim 20 \text{ arcsec}$ resolution which is unattainable with *Herschel*/SPIRE 350 and 500. *Laboca* is a multi-channel bolometer array for continuum observations at $870 \mu\text{m}$ installed on the Atacama Pathfinder Experiment (APEX) telescope

¹ We use the formalism of the mass function – $\log_{10}(N(\Delta \log_{10}(m)))$ versus $\log_{10}(m)$ – as given by Scalo (1986). In this definition the Salpeter mass function has a slope of -1.35 and the Kroupa mass function has a slope of -1.3 above $0.5 M_{\odot}$.

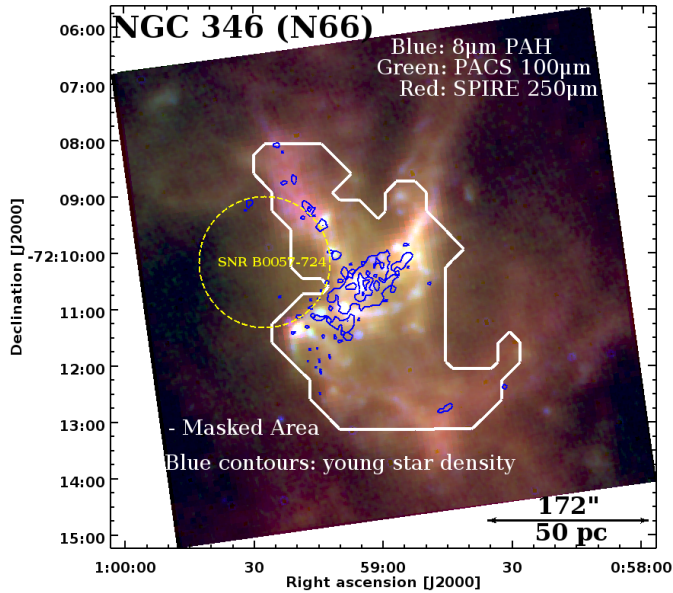


Figure 2. False colour image showing an overview of the large environment of NGC 346 in key ISM tracers. We show $8\ \mu\text{m}$ emission indicative of the location of the most prominent PDRs (blue; IRAC4 emission minus the stellar continuum estimated from IRAC2), the warmer dust traced by PACS 100 (green) and the cooler dust (SPIRE 250, red). Each waveband is shown at its native resolution. The blue contours show the stellar density (see Fig. 1). The general observed trend is a decreasing dust temperature with distance to the most rich cluster (yellow to red colour gradient) and strong PDRs near (but not peaking on) the stellar concentrations. The region where both dust surface density, including *Laboca* measurements, and stellar densities are well defined is indicated by the white line (see Sect. 3.4 for details).

in Chile. It has a field-of-view of 11.4 arcmin and a PSF full-width-at-half-max of $19.2 \pm 0.3\text{ arcsec}$. Observations of the NGC 346 region with *Laboca* were carried out in December 2008 and April, May and September 2009 (Program ID: O-081.F-9329A-2008 PI: Hony). The mapping was done with a raster of spiral pattern in order to fully sample the final map (size of the region mapped: $25 \times 25\text{ arcmin}^2$). Data are reduced with the BOLometer Array Analysis Software (BoA Schuller et al. 2010). The scans are reduced individually. They are calibrated using the observations of planets (Mars, Neptune, Uranus, Venus) and secondary calibrators (G10.62, G5.89, HLTAU, PKS0506.61, PMNJ0210-5101, PMNJ0303-6211, PMNJ0450-8100, N2071IR and VY-CMa). We determine zenith opacities using a linear combination of the opacity determined using sky-dips and that computed from the precipitable water vapor². We remove dead or noisy channels as well as stationary points or data taken at fast scanning velocity or above an acceleration threshold. We subtract the correlated noise, apply steps of median noise removal, baseline correction and despiking. The reduced scans are then combined into a final map. We isolate the pixels above a given signal-to-noise ratio to define a ‘source model’ that is subtracted from the time-ordered data. We rerun the reduction pipeline and add the source model to the time-ordered data to obtain a new map. The process is iterated until the result map converges (5 iterations were applied for NGC 346)³. The final

² Tabulated sky opacities are provided at <http://www.apex-telescope.org/bolometer/laboca/calibration>

³ More details on the techniques are provided in Galametz et al. (2013).

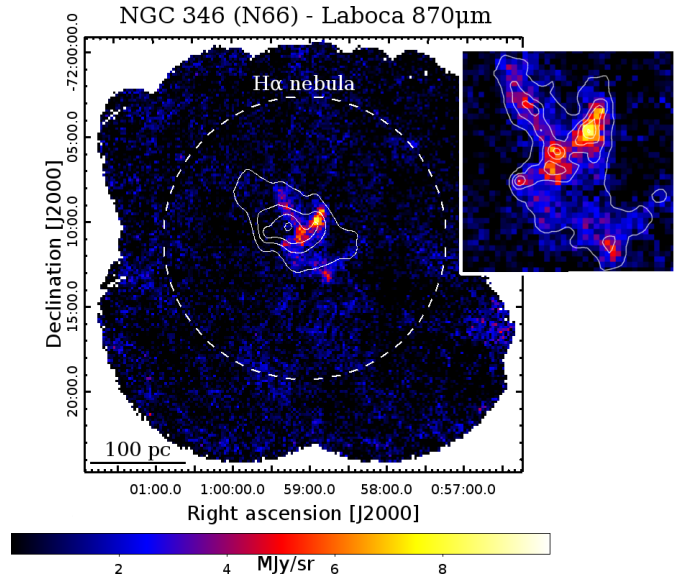


Figure 3. *Laboca* $870\ \mu\text{m}$ map of NGC 346. The contours show the 36 cm radio continuum emission from SUMSS (Mauch et al. 2003). The 3 and 6 cm radio continuum images (not shown) exhibit the same morphology (Dickel et al. 2010). The possible corresponding contribution of free-free emission at $870\ \mu\text{m}$ has been filtered-out by the median filtering applied in the data reduction process. The dashed circle indicates the approximate extent of the $\text{H}\alpha$ nebula. We show a close-up of the brightest region in the inset, in which the $250\ \mu\text{m}$ dust emission contours, in perfect correspondence with the *Laboca* map, are shown.

map is shown in Fig. 3. Within the region of interest there are three main emission features. There is an emission peak towards the central cluster, a direct indication that this sight-line is dust rich. We detect a brighter emission peak towards the north-west of the main cluster and a plume of $870\ \mu\text{m}$ emission which follows the string of stellar clustering towards the north-west. This plume coincides with the brightest CO($j=2-1$) emission detected in the region Rubio et al. (2000). Due to the median filtering that is applied to remove the atmospheric and telescope signal, any spatially very extended emission has been removed as well. This explains why we do not detect any free-free emission from the ionized gas which should be present in this region (see Fig. 3)

3.4 Beam matched data

In our analysis, we use maps with a resolution of 20 arcsec (6 pc at the distance of the SMC). All maps with intrinsic spatial resolutions better than this resolution, including the stellar catalogue, have been convolved to the this effective spatial resolution. *Laboca*, MIPS 70 and SPIRE 250 maps have not been convolved since they already have an intrinsic spatial resolution very close to 20 arcsec . We use the convolution kernels available from Karl Gordons web page⁴ for convolving to the SPIRE 250 beams. For the stellar density map – which has an exceedingly good intrinsic angular resolution we have directly convolved the 2 arcsec stellar density map with the SPIRE $250\ \mu\text{m}$ beam. After convolution, all maps have been re-projected on the same pixels scheme with pixels the size

⁴ http://dirty.as.arizona.edu/~kgordon/mips/conv_psfs/conv_psfs.html

of $20 \times 20 \text{ arcsec}^2$ in order to have spatially independent measurements and to allow pixel-by-pixel SED extraction and comparison between the stellar densities and derived dust surface densities. We use the program *swarp* from AstroMatic⁵ for calculating the re-projected maps, as it is in our experience the most accurate tool in conserving the mean surface brightness. This is particularly true when re-projecting to a pixel scheme with very different pixel sizes, which is our case⁶.

In order to create reliable random noise maps that represent well the noise in the original maps and the effects of convolution and re-projection we apply the following procedure:

- The amplitude of the noise in each map has been estimated by measuring the median absolute deviation from the median (MAD). This value is a more robust measure of the noise in a map than the standard deviation in the presence of real source emission. The estimated standard deviation equals $1.4825 \times \text{MAD}$.
- We generate a pure noise map at the original resolution using the measured standard deviation.
- We generate a projected noise map convolving and re-projecting this noise map in the exact same manner as we do the science map.
- We measure the amplitude of the noise in the projected noise map as the standard deviation of the fitted Gaussian function to the histogram of pixel values.

These output noise levels have been compared to the formal calibration uncertainties (expressed as percentages of the observed surface brightness levels). For all maps except the *Laboca* map, the absolute calibration is dominant throughout the region of interest. In the case of the *Laboca* map, we retain for each pixel in the projected noise map the larger value of the flux calibration uncertainty and the random noise value. These uncertainties should not be added (quadratically) because the *Laboca* flux calibration uncertainty reflects the scatter in the measured calibrator fluxes and is thus, in essence, also a random noise term.

Pixels outside the area surveyed by *HST* and pixels where the *Laboca* measurement is less than 2σ are masked. There are 115 valid, independent $20 \times 20 \text{ arcsec}^2$ pixels (covering about $\sim 4000 \text{ pc}^2$) in the following pixel-by-pixel analysis. Their outline is shown in Fig. 2. All maps at the other wavelengths have signal-to-noise ratios larger than 2 – in most cases much larger – in these pixels.

4 DUST, GAS AND SFR SURFACE DENSITIES

4.1 SED fitting

In order to derive dust surface densities, we fit the IR to submm dust continuum SED for each independent pixel in the region. The dust emission fitting is performed with the Galliano et al. (2011a) SED model. This model accounts for variations of dust excitation rates along the line-of-sight. Following the prescription of Dale et al. (2001), it assumes that the distribution of dust mass, M_d , is parametrized by the starlight intensity, U , as a power law: $dM_d/dU \propto U^{-\alpha}$, between U_{min} and $U_{min} + \Delta U$. The parameter U is the stellar flux received by the dust and is normalised to the solar neighbourhood value (Mathis, Mezger & Panagia 1983). The

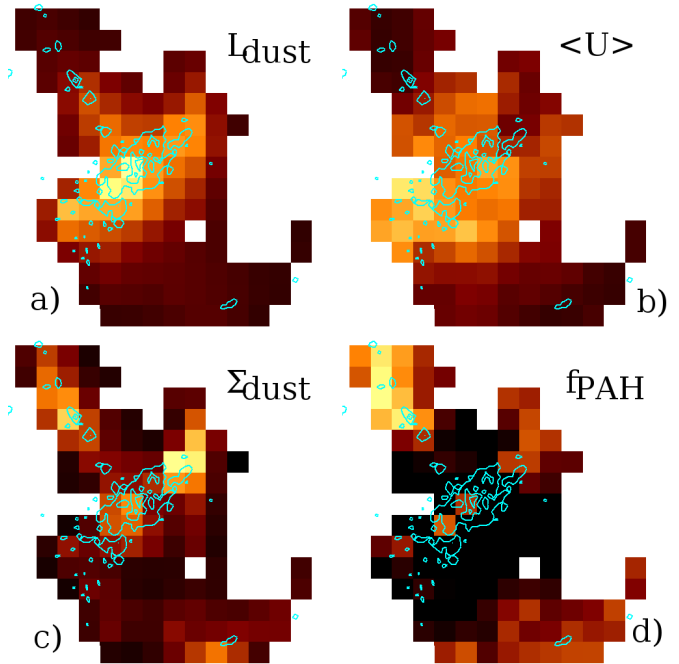


Figure 4. Maps of the output parameters of the dust SED fitting. The region shown corresponds to the white contour in Fig. 2. For reference we show the surface density map of young stars in contours (see Fig. 1). We show the luminosity of the dust emission ranging from 150 to $1300 L_{\odot}$ (a), the average radiation field as experienced by the dust ranging from 6 and $45 G_0$ (b), dust surface density ranging from 0.05 to $0.3 M_{\odot} \text{ pc}^{-2}$ (c) and the mass of PAHs relative to the total dust mass normalised to the Galactic value ranging from 0 to 0.3 (d).

shape of the SED (in particular, both its peak wavelength and its width) constrain the parameters of this power law.

For a given starlight intensity, U , the dust emissivity is derived from the Zubko, Dwek & Arendt (2004, dust family: BARE-GR-S) model, designed to fit the diffuse Galactic emission. However, we replace graphite by amorphous carbon (Zubko et al. 1996, ACAR). Indeed, Galliano et al. (2011a) showed that the standard Galactic grain properties applied to *Spitzer* and *Herschel* observations of the LMC lead to violation of elemental abundance constraints, while the modified composition (the ‘AC model’) gives realistic gas-to-dust mass ratios. In summary, we make the assumption that grains in the SMC will have similar optical properties as in the LMC.

The choice of a set of grain emissivities is tainted by systematic uncertainties. As demonstrated by Galliano et al. (2011b), the derived dust mass change by a factor of 2 to 3 depending on the optical properties. However, it is also shown that the change is essentially a simple scaling of the dust mass, and do not significantly affect the trends. Besides, if the origin of the difference in emissivity between the Milky Way and the LMC is an evolutionary effect, linked to metallicity (cf. Planck Collaboration et al. 2011), it is likely that using LMC emissivities puts us closer to the reality than simply assuming Galactic properties.

The fit of the observed SED, with the previously described dust model, provides constraints on: the dust mass, M_d ; the parameters of the power law distribution of starlight intensities, U_{min} , ΔU and α , which we summarise by quoting the average starlight intensity, $\langle U \rangle$; and the PAH mass fraction, normalised to the Galactic value, f_{PAH} . In order to estimate the final uncertainties on these derived dust parameters, we perform Monte-Carlo iterations, fol-

⁵ <http://www.astromatic.net>

⁶ The IDL/astrolib tool *hastrom*, often used for the same purpose, performs poorly in this case.

Table 2. Total dust mass, gas consumption time-scale and integrated SFE as a function of the area considered in the analysis. The first row corresponds to the area included in the pixel-by-pixel analysis. A radius of 52 pc is equivalent to the area covered by the *HST* observations. The 90 pc radius matches the prominent SPIRE 250 and 350 μm waveband emission, while the largest radius probes the full extent of the $\text{H}\alpha$ nebula around NGC 346. The gas consumption time-scale (τ_{gas}) is defined as the $M_{\text{gas}}/\text{SFR}$ and the integrated star-formation efficiency ($\text{SFE}_{10\text{Myr}}$) is calculated as the percentage of gas that will have been converted into stars after 10 Myr, assuming that the SFR remains constant. We use 10 Myr as the limiting age, when supernovae might disrupt the ISM and halt the star formation.

area/radius	M_{dust} [M_{\odot}]	τ_{gas} [10^8 yr]	$\text{SFE}_{10\text{Myr}}$ [%]
mask	$498 \pm 18\%$	1.7	5.8
52 pc	$900 \pm 19\%$	2.5	4.0
90 pc	$1616 \pm 19\%$	4.5	2.2
145 pc	$2741 \pm 22\%$	7.6	1.3

lowing the method described in Galliano et al. (2011a), taking into account the correlation between calibration uncertainties. The median uncertainties on the derived parameters (σ_x/x) are 6 per cent for L_{dust} , and 19 per cent for Σ_{dust} and $\langle U \rangle$. The median standard deviation on f_{PAH} is 0.02.

Maps of the best fit output parameters are shown in Fig. 4. One of the key results from the SED fitting which is evident from these maps is the clear distinction between the parameters which trace the heating of the dust (panels a and b) and the surface density of dust (panel c). Clearly the dust luminosity in the very active star forming region NGC 346 (panel a) traces closely the radiation field. This is in stark contrast to other (more usual) observations of more diffuse regions where the incident radiation field (and dust temperature) does not vary much and L_{dust} traces the dust surface density. Panel d shows that the PAH abundance close to the main cluster is so low that their emission is undetectable in the broadband photometry. This low abundance of PAH is in perfect agreement with the findings of Sauvage, Vigroux & Thuan (1990) who deduced an increased differential depletion of PAHs towards NGC 346 based on IRAS photometry. Similar paucities of PAHs towards other high-mass star forming region in the Magellanic Clouds have been reported (e.g. Sandstrom et al. 2010; Hony et al. 2010).

4.2 Conversion of dust surface density to gas surface density

We assume that gas and dust are well mixed along each line-of-sight in which case the gas surface density (Σ_{gas}) is proportional to the dust surface density (Σ_{dust}) and the proportionality factor is the gas-to-dust mass ratio (r_{gd}). The dust masses derived by SED fitting methods vary significantly and systematically (e.g. Galliano et al. 2011b; Gordon et al. 2014) depending on the applied method and assumed dust optical properties. It is therefore important to use a value of r_{gd} consistent with the used SED fitting methodology, i.e. the value of r_{gd} that gives the correct gas mass given the derived dust mass. We have calibrated the r_{gd} using the available gas tracers on a large scale. Within a 500 arcsec radius centred on NGC 346 we find an atomic gas mass of $2.7 \cdot 10^6 \text{ M}_{\odot}$ using the Parkes+ATCA HI map (Kim et al. 2003) and a spin temperature of 60K (Bernard et al. 2008). The molecular gas mass determined from CO(J=1-0) within the same aperture is $7.4 \cdot 10^4 \text{ M}_{\odot}$ when using a CO-to- H_2 column density conversion factor (X_{CO})

of $10^{21} [\text{cm}^{-2} (\text{K km s}^{-1})^{-1}]$ (Bolatto, Wolfire & Leroy 2013). If we use an X_{CO} of $10^{22} [\text{cm}^{-2} (\text{K km s}^{-1})^{-1}]$ we find a molecular gas mass of $7.5 \cdot 10^5 \text{ M}_{\odot}$. Such an elevated X_{CO} may be more appropriate given the harsh radiation field that is prevalent in the region, which may induce enhanced photo-dissociation of the CO molecules. Thus, we derive a total gas mass in the range of $2.7 \cdot 10^6$ to $3.4 \cdot 10^6 \text{ M}_{\odot}$. The dust mass derived using the dust continuum photometry in this aperture and applying the same SED fitting routine we use for the pixel-by-pixel analysis yields $2.7 \cdot 10^3 \text{ M}_{\odot}$. The derived r_{gd} ranges from ~ 1000 to ~ 1250 . In the following we use a fiducial value for r_{gd} of 1250, which is much higher than the Galactic value (100, Draine & Li 2007) due to the lower metallicity of the SMC. Our value for r_{gd} of 1250 is lower than the total SMC integrated value of 1740 from Gordon et al. (2014). The global value includes a significant amount of atomic gas at low column density in the outskirts of the SMC which is not detected in dust emission. This drives up the global r_{gd} .

Given that the derivation of r_{gd} is susceptible to significant *systematic* uncertainties in X_{CO} for the gas surface densities and dust optical properties for the dust surface densities, we will discuss the implications of a factor of two variations in the absolute value of r_{gd} on our results. Note that, part of the purpose of this paper is to determine how well the ISM and stars follow each other on small spatial scales. This part of the analysis does not depend on the chosen absolute value for r_{gd} . The comparison of SFR and star-formation efficiencies with values derived for other regions is however sensitive to the chosen value and we will discuss the influence of our choice on the results we find.

We further assume r_{gd} to be invariant for the entire region. In principle, it is possible that r_{gd} could vary significantly, in particular in the vicinity of high-mass star-formation sites, where dust destruction can become important due to supernovae explosions. Reid et al. (2006) have studied the supernovae remnants within the large environment of NGC 346. These authors show that the region we study here appears largely unaffected by the impact of supernovae. The closest remnant they identified (SNR B0057-724, see also Fig. 2) lies to the North-East of the main cluster, outside of the region of interest. The observational data argue against strong variations of r_{gd} because they show that the ratio of dust heating compared to gas heating is very constant throughout the whole region (see Sect. 6.2).

4.3 Star formation rate surface densities

The star-formation-rate map has been derived using the observed number of young stars along the line-of-sight in each pixel of the beam-matched stellar density map. It is calculated as (see also Table 1):

$$\text{SFR} = \frac{N_{\star} M_{\text{cat}}}{\Delta t_{\text{SFR}}} = \frac{N_{\star} \cdot 4.3}{5 \cdot 10^6} [\text{M}_{\odot} \text{ yr}^{-1}] \quad (1)$$

The star-formation surface density map (Σ_{SFR}) is obtained by dividing this map by the area of a pixel in kpc^2 .

In Fig. 5, we compare the derived Σ_{SFR} with selected, indirect star-formation rate tracers. Note that we only compare with those tracers ($\Sigma_{\text{H}\alpha}$ —calibration from Hao et al. (2011) for a Kroupa IMF; $\Sigma_{24\mu\text{m}}$ —calibration from Rieke et al. (2009) and Σ_{TIR} —calibration from Murphy et al. 2011) which are appropriate for the very recent epoch of star-formation ($< 5 \text{ Myr}$) and we do not consider FUV because its calibration assumes a constant SFR over $> 10\text{--}100 \text{ Myr}$. As can be seen, the Σ_{SFR} from star counts is generally higher than those obtained from $\text{H}\alpha$ or dust emission. Moreover, the differ-

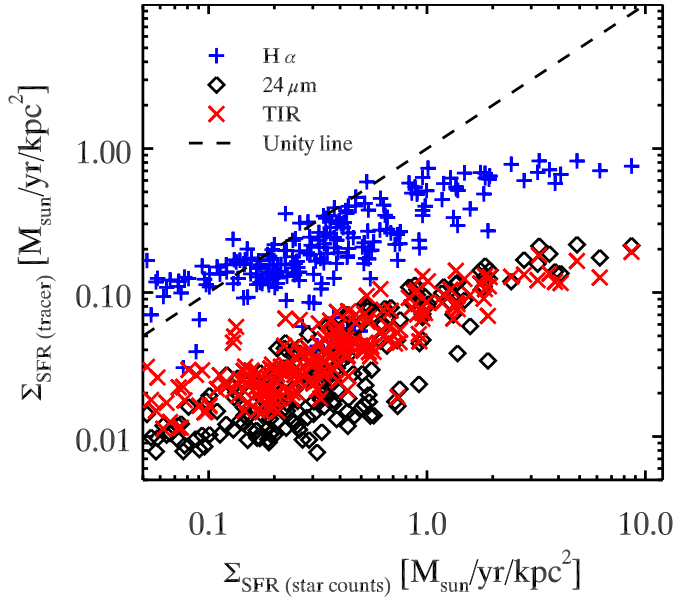


Figure 5. Comparison of derived pixel-by-pixel Σ_{SFR} using different methods. The x-axis shows the Σ_{SFR} using the young-star surface density. In blue we show Σ_{SFR} calculated following Hao et al. (2011, for the Kroupa IMF) using the continuum subtracted $\text{H}\alpha$ map from MCELS (Smith, Leiton & Pizarro 2000) that was kindly provided by S. Points. The red crosses are Σ_{SFR} estimates using the total infrared (TIR) (3–1100 μm) surface brightness following Hao et al. (2011) and the black symbols show the estimated Σ_{SFR} based on *Spitzer*/MIPS 24 μm (Rieke et al. 2009).

ences are largest where the stellar density (i.e. Σ_{SFR}) is highest. Towards the densest cluster the difference between counting stars and using $\text{H}\alpha$ is a factor of 10, while the dust tracers yield a *local* Σ_{SFR} lower by a factor of 50. The dust tracers yield much lower values (by a factor of ~ 5) than both $\text{H}\alpha$ due to the reduced dust abundance in the SMC.

The origin of the weak dust emission in NGC 346 is not the same as the weak emission in the Gould-belt star-formation regions reported by Vutisalchavakul & Evans (2013). These authors have compared the SFR one would derive from *Spitzer*/MIPS 24 μm measurements or TIR with SFR derived from counting YSOs. They find that the IR tracers underpredict the true star formation rate by two orders of magnitude, because these regions lack high-mass stars due to incomplete sampling of the initial mass function. NGC 346 is a very rich environment and does not have such a lack of high-mass stars.

The difference between young star counts and the $\text{H}\alpha$ derived values is due to the fact that the individual massive young stars in NGC 346 produce $\text{H}\alpha$ (and dust) emission over a much larger surface than the size of the pixel in which they are counted, significantly larger than the full *HST* field-of-view. Note, that this effect will cause the tight relation between SFR (derived from $\text{H}\alpha$) and the gas column density to break down on small ($\lesssim 100$ pc) scales, similar to what is observed in M33 (Onodera et al. 2010). This break-down occurs even in the absence of drifting of the stars from their birth environment or spread induced by evolutionary effects, simply because the local $\text{H}\alpha$ (or dust) emission no longer measures the locally produced UV-radiation field. Figure 6 demonstrates how large this distance is. We show the fraction of the SFR which is recovered when integrating the extinction corrected $\text{H}\alpha$ emission (based on the combination of $\text{H}\alpha$ and 24 μm emission) in apertures of increasing radius. Within the *HST* field-of-view we recover 50

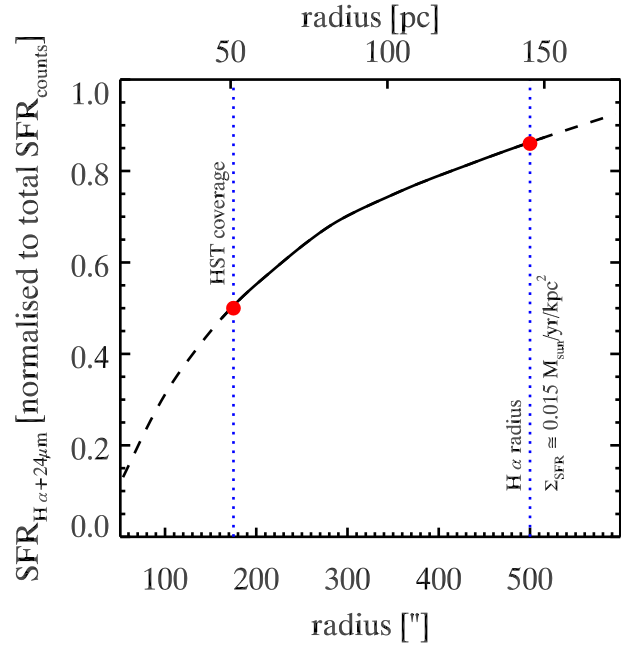


Figure 6. Derived total SFR for the NGC 346 complex based on the combined emission of $\text{H}\alpha$ and 24 μm as function of the radius (centred on $14.776^\circ; -72.1735^\circ$) over which the flux is integrated. We follow the prescription from Calzetti et al. (2007, Eqn. 5). The SFR is expressed in terms of the fraction of the total SFR derived from star counts. The $\text{H}\alpha$ and 24 μm emission are much more extended than the distribution of the young stars. As can be seen, the SFR derived within the radius of the *HST* coverage (~ 50 pc) is about half of the total SFR. Only when we integrate over the complete nebula (~ 500 arcsec), where the $\text{H}\alpha$ emission reaches the diffuse background level do we derive similar SFR values.

per cent. When we integrate out to a radius of 500 arcsec (145 pc), where the $\text{H}\alpha$ emission from the NGC 346 complex becomes indistinguishable from the general SMC emission, we recover ~ 90 per cent. In this calculation we assume that outside the field-of-view of the *HST* observations, the star formation is insignificant. This is corroborated by the results of Sewilo et al. (2013) who identified YSO candidates based on IR photometry of the entire SMC. Of the sources from their highly-reliable YSO-candidate list which are associated with NGC 346, less than 20 per cent (4/23) are located outside of the field-of-view of *HST*. A very similar result is found when using the spectroscopically confirmed early-type stars from Bonanos et al. (2010). Of the 43 O-type stars from this catalogue within a 100 pc radius around NGC 346 only ~ 15 per cent (6) are not within the field-of-view of *HST*.

We conclude that the total SFR as measured from the (predominantly low-mass) young star counts is consistent with the SFR measured from $\text{H}\alpha$ emission to within ~ 10 per cent. However, the absorption of the hard radiation from the hot stars and subsequent re-emission as either recombination lines or dust continuum occurs far – at distances > 100 pc, in the case of NGC 346 – from the actual location of these stars. See also Relaño et al. (2012) and Li et al. (2013) for excellent discussions on how radiation escaping the local environment affects $\text{H}\alpha$ and dust emission as SFR tracers on small spatial scales. As a consequence, these indirect tracers which depend on absorption and re-emission, cannot be used for our present purpose, which is to relate the stellar densities with the ISM on smaller scales within the star forming complex. Note that most extra-galactic studies that use $\text{H}\alpha$ to derived SFR are probing

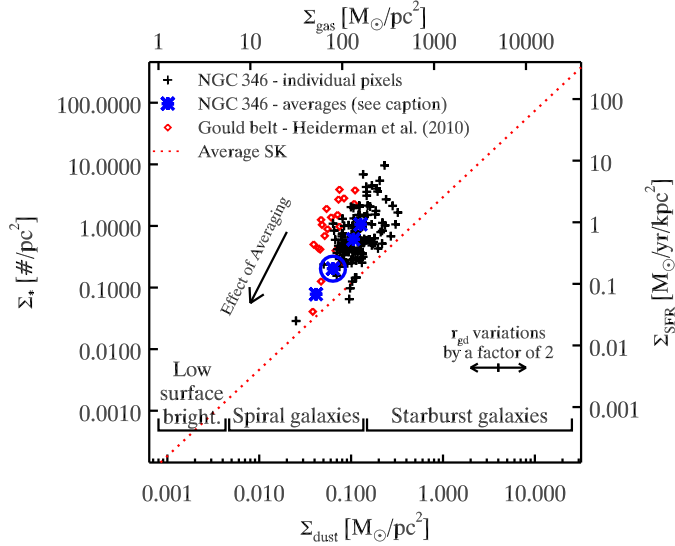


Figure 7. Scatter plot of surface density of young stars versus surface density of dust per pixel of $20 \times 20 \text{ arcsec}^2$ ($6 \times 6 \text{ pc}^2$). The dotted line shows the ‘standard’ relation from Kennicutt & Evans (2012, Fig. 11a). The values from Heiderman et al. (2010), based on YSO counts and ISM column densities in nearby individual molecular clumps, are also shown. The values for NGC 346 (black pluses) lie systematically above the ‘standard’ line. The thick blue stars indicate where NGC 346 is located when we average over all pixels in the masked area, and subsequently over apertures with radii of 52, 90 and 145 pc (from top-right to bottom left). These radii correspond to the approximate size of the HST surveyed area, the prominent far-IR emission nebula and the size of the $\text{H}\alpha$ nebula, respectively. The power law exponent of the effect of averaging, i.e. the slope of the arrow in the figure, is 2.9.

much larger regions ($\gtrsim \text{kpc}$) than the scale on which the indirect tracers are reconciled with the direct measurements ($\sim 150 \text{ pc}$) and are thus unaffected by this effect.

5 COMPARISON OF GAS AND STARS

In the following section, we compare the derived SFR and ISM column densities. We first concentrate on the global behaviour and how NGC 346 compares to other measurements before looking in more detail at the tendencies within the complex.

5.1 Global comparison

We show in Fig. 7 the stellar surface density versus the dust surface density for each pixel. These are the basic observational quantities which do not depend on assumptions about M_{cat} , Δt_{SFR} or r_{gd} . Using the values in Table 1 we convert these into Σ_{SFR} and Σ_{gas} (right and top axes). The individual pixels within NGC 346 lie above the fiducial SK-relation for Σ_{SFR} versus $\Sigma_{\text{HI}+\text{H}_2}$ (Kennicutt & Evans 2012, Fig. 11a) by on average a factor of 7. For reference, we also show the points for individual clumps in nearby Milky Way star forming regions from Heiderman et al. (2010), which also lie consistently above the SK-relation. These authors use SFR from low-mass YSOs and column densities from the dense gas measured from extinction maps on a typical scale of a few parsec. The fact that all these small-scale measurements lie above the galaxy averaged values is expected (Kruijssen & Longmore 2014). The offset is due to the selection biased introduced by studying a region

which is currently, actively forming stars, while the galaxy averaged values include also regions which are not presently forming stars. Compared to the study from Heiderman et al. (2010), our approach has the advantage of using the dust in *emission* to measure the column densities and that we have access to dust emission covering a large area surrounding the star forming complex. This allows us to calculate averaged values over relevant spatial scales, taking into account also parts of the ISM which are less vigorously forming stars.

The thick blue stars correspond to averages over the entire masked area, the entire *HST* field-of-view, the prominent SPIRE 250 μm emission and the $\text{H}\alpha$ nebula (top-right to bottom left, respectively, see also Tab. 2). The mean value lies progressively closer to the SK-relation as we increase the area over which we calculate the average. It should be noted that the same shifting to bottom left *must* occur also to the values from Heiderman et al. (2010) if they were to integrate to larger distance from their young stars (to lower column densities), as the conditions that prevail in their low-mass star forming regions are probably more representative for the spiral galaxies at low Σ_{SFR} rather than those on the dividing line between the most active spirals and star burst galaxies. The third star from the top in Fig. 7 – highlighted by a circle – indicates the average over the area where significant cold dust emission is detected in excess to the general SMC emission. This is probably the best estimate of the average SFR and ISM column density for the complex in its entirety. This value is above the SK-relation by about a factor of three albeit roughly compatible with the average relation when taking into account its scatter of 0.3dex. This factor is consistent with the prediction from Kruijssen & Longmore (2014) for the size of the region $\sim 300 \text{ pc}$ diameter over which we do the comparison. We also indicate in Fig. 7 by how much the NGC 346 values would be displaced (left-to-right) relative to the data from Heiderman et al. (2010) and the SK line as a result of a factor of two variations in r_{gd} . If r_{gd} were 2500 as opposed to 1250, the average values of NGC 346 would fall on the SK line. Such a high value for r_{gd} would imply that half of the total gas (more than 80 per cent of the molecular gas) within a 500 arcsec (145 pc) radius around NGC 346 is molecular without corresponding CO emission, as a result of photo-dissociation of the CO molecule. Such an large reservoir of hidden molecular gas, not related to CO, seems difficult to reconcile with the emission of C^+ which traces the photo-dissociation. Israel & Maloney (2011) show that the distribution of the $[\text{C II}]$ 158 μm line emission closely resembles the CO distribution.

5.2 The physical origin of variations in stellar mass fraction

On the spatial scale that we probe here ($\sim 6 \times 6 \text{ pc}^2$) we measure significant scatter in the relation between Σ_{gas} and Σ_{M_\star} (Fig. 7). Such scatter on small scales is expected, due to the stochastic nature of the local star-formation process, as well as relative motions between the formed stars and the reservoir from which they formed (Kruijssen & Longmore 2014). The observed scatter is more easily assessed in Fig. 8, where we concentrate on the values derived for NGC 346. This figure also shows the derived power law for the entire ensemble of sight-lines. We use the IDL routine MPFITEXY⁷ (Williams, Bureau & Cappellari 2010) which uses MPFIT Markwardt (2009) to determine a straight-line fit to the data (in log-log space) with uncertainties in both variables. The best fit value for the exponent is 2.6 ± 0.2 , i.e. the relation is much steeper than the

⁷ <http://purl.org/mike/mpfitexy>

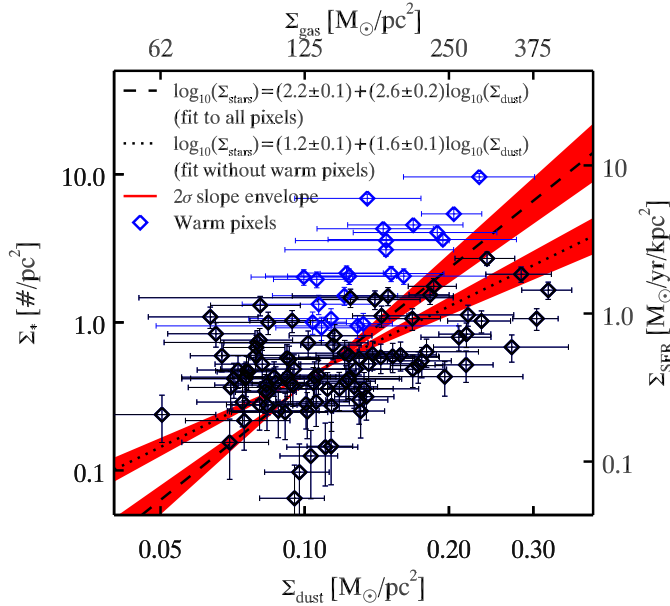


Figure 8. Scatter plot of surface density of young stars versus surface density of dust per pixel of $20 \times 20 \text{ arcsec}^2$ ($6 \times 6 \text{ pc}^2$) zoomed in on the range occupied by NGC 346. The blue points have a strong warm dust component in their SED ($\Sigma_{24 \mu\text{m}}/\Sigma_{250 \mu\text{m}} [F_\nu/F_\nu] > 0.3$). Clearly, the lines-of-sight selected using this colour criterion occupy a separate region of the diagram. The long and short dashed lines are the straight-line fits in logarithmic space to the data with or without the warm pixels, respectively. The red areas corresponds to the 2σ uncertainties of the best-fitting slope, while keeping the normalisation fixed.

canonical SK-relation (exponent: ~ 1.4). This very steep increase of Σ_{SFR} with Σ_{gas} is similar to the large exponents found by Gutermuth et al. (2011).

The observed variations in SFR at higher dust/gas surface densities are clearly correlated with other observables, in particular the dust colour-temperature (here $\Sigma_{24 \mu\text{m}}/\Sigma_{250 \mu\text{m}} [\text{Jy/Jy}]$). Perusal of the data shows that those pixels with $\Sigma_{24 \mu\text{m}}/\Sigma_{250 \mu\text{m}} > 0.3$, i.e. warm dust, are towards the rich stellar cluster and all exhibit high values in this diagram. The position of these warm sight-lines is also indicated in Fig. 9. We further show the power law fit to the data excluding the lines-of-sight with this very warm dust (exponent 1.6 ± 0.1). The derived exponent of the power law varies significantly depending on whether we include these sight-lines, which is an indication that the lines-of-sight towards the main cluster occupy a particular part of this diagram.

It is interesting to note that the rms scatter around the best-fitting power law is $\pm 0.4 \text{ dex}$. This is similar to the rms observed ($\pm 0.3 \text{ dex}$) in the SK-relation of integrated ‘normal’ spiral galaxies (Kennicutt & Evans 2012). Perhaps, some of the differences in physical conditions that underpin the variations among spiral galaxies are encountered within the NGC 346 star forming complex. If this is indeed the case, then studies such as the one we present here, offer a rare opportunity to zoom in to specific environments and determine the parameters that drive such variations.

In the following we discuss the variations in terms of the stellar mass fraction of young stars ($\text{frac}_{\text{M}_*} = \Sigma_{\text{M}_*} / (\Sigma_{\text{M}_*} + \Sigma_{\text{gas}})^{-1}$) to facilitate comparison with star cluster formation models, where Σ_{M_*} refers to the mass of the PMS+UMS stars. Moreover, we prefer this terminology over star formation efficiency, which concerns the time averaged rate with which a large quantity of interstellar matter (entire complexes) is converted into stars. On the small

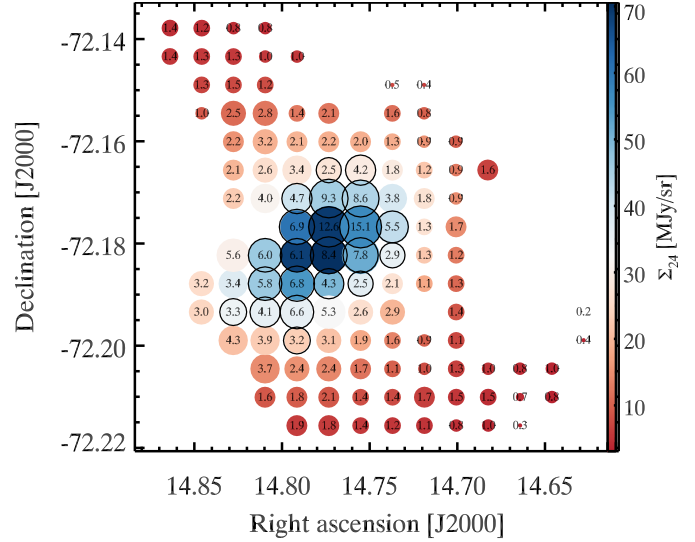


Figure 9. Map of the NGC 346 which shows the derived stellar mass fraction. The size of each point is dependent on frac_{M_*} and its colour depends on $\Sigma_{24 \mu\text{m}}$. The mass fraction is indicated in each point. It is clear from this diagram that the stellar mass fraction peaks on the stellar cluster where the dust is heated to higher temperatures due to the intense radiation field. The warm pixels identified in Fig. 8 are encircled.

scales we probe here, we measure the stars that have formed earlier and the remaining ISM column density. It is not evident that these stars have formed from the ISM we detect now along the line-of-sight nor that they will still be in this location, if and when the next generation of stars is born.

Across most of the surveyed area (66 per cent of the pixels) frac_{M_*} is below 2 per cent, with the most common value being 1 per cent⁸, see also Fig. 9. However, there is a significant tail to much higher values with a maximum of 15 per cent. These very high values correspond to very high stellar surface densities, *not* to low ISM column densities (see Fig. 4).

The observed variations in frac_{M_*} are certainly not random, but show a definite dependence on other measurable quantities. In particular, the highest values are found near the main cluster (Fig. 9). We also show the trend of stellar mass fraction as a function of distance to the main cluster in Fig. 10. Even though there are clear deviations from spherical symmetry in the region, we observe a monotonic decrease in frac_{M_*} with distance which can be approximated by a power law with exponent -0.7 .

From the observations and the SED fitting, we have at our disposal a number of key probes that typify the conditions along the line-of-sight of each pixel. These range from quantities that measure directly the stellar densities and the resulting intense radiation field, to those that depend on both the local radiation field and the ISM column density and state. In these same ordering, these probes are: Σ_* , $\Sigma_{24 \mu\text{m}}$, the average radiation field ($\langle U \rangle$) as experienced by the dust grains⁹, Σ_{gas} , the molecular gas fraction and the molecular gas surface density. Perusal of the data shows that frac_{M_*} correlates well with stellar densities and hot dust emission at $24 \mu\text{m}$

⁸ 1 per cent corresponds to a gas consumption time-scale of $5 \cdot 10^8 \text{ yr}$, given the duration of the star-formation event of 5 Myr

⁹ $\langle U \rangle$ is the average field weighted by dust mass and as a result does not measure the ambient radiation field if the line-of-sight extinction is significant.

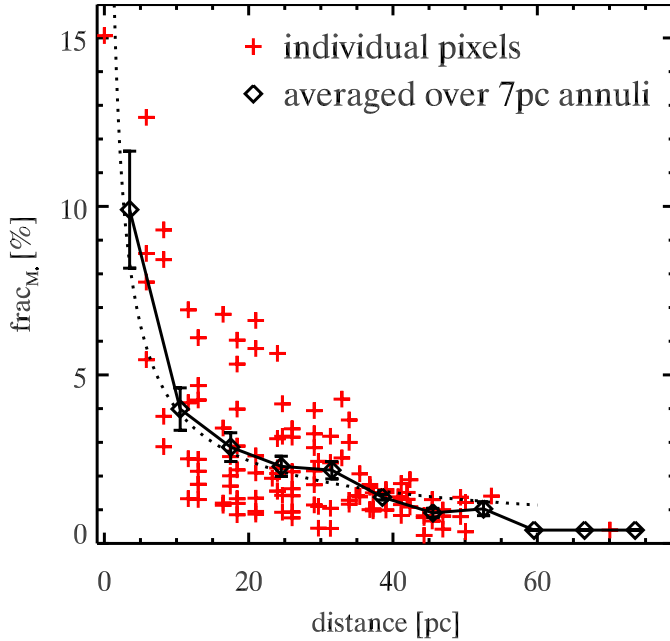


Figure 10. Trend of stellar mass fraction as a function of distance from the main cluster (ra=14.755179°, dec=-72.171201° [J2000]). Individual pixel values are shown by red pluses. Annular-averaged values (in steps of 7 pc) are shown with black diamonds. The error bars shown are 1σ uncertainties on the mean. The behaviour can be approximated by $frac_{M\star} [\%] = 20 \cdot \text{distance} [\text{pc}]^{(-0.7)}$ between ~ 1 and 55 pc (dashed line).

(Fig. 11,a,b). The correlation with the ISM column density is much less tight (panel c), which is in part due to the fact that the amplitude of variations in Σ_{gas} are much smaller than those in Σ_{\star} , i.e. the gas map is much flatter than the star map. When we use $\Sigma_{\text{CO}}/\Sigma_{\text{gas}}$ as a proxy for the molecular gas fraction (panel d), there is no obvious correlation between the stellar mass fraction and the molecular gas fraction. Specifically, the highest and the lowest stellar mass fractions coincide with intermediate values of the molecular gas fraction. The same is true also for the molecular surface density (panel e).

The basic conclusion we can draw is that the highest stellar mass fractions are found where the highest concentrations of stars are found, towards the central cluster. *There are many stars where there are many stars.* We find no obvious parameters of the current ISM towards the cluster that explain why the cluster formed there. It is neither the densest nor the most molecular ISM within the complex. Probably the strong radiation over the past few Myr has already erased the memory of the conditions that led to the formation of the cluster.

It should be noted that the central location of the main cluster may be a clue to why it formed there. It truly is central to the complex in most tracers. In the ISM column density tracers, in particular, the main cluster location appears as the intersecting ‘hub’ of three peripheral dense ‘arms’ (Fig. 2 and 12). If the main cluster is indeed located at the meeting point of several dense arms, it is possible that the star formation process was/is being fed by these structures. Whether this is the case cannot be assessed without kinematic measurements of the dense gas.

6 POSSIBLE BIASES

We find that the stellar mass fraction is highest towards the rich central cluster. There are several effects and biases that could influence this interpretation.

6.1 Completeness

The derived relation between the newly formed stars and the ISM depends on the completeness of the *HST* stellar catalogue. The average completeness for stars which are too faint and crowding has been accounted for by integrating the completeness corrected mass function (Sabbi et al. 2008, see also Sect. 3). If there are remaining incompleteness issues in the catalogue, the $frac_{M\star}$ would be even higher than we derive now. The observed variations in $frac_{M\star}$ could be affected, if there are large spatial variations in completeness.

Crowding: The regions which could be affected by crowding more than the average are the regions of the highest stellar density. However, these regions already have the highest mass fraction of stars, and an additional correction would place these regions farther from the mean rather than closer.

Extinction: NGC 346 exhibits some sight-lines with significant amounts of dust (Fig. 12) which could hide embedded clusters of young stars. This could affect, in particular, the regions labelled #3 and #4. Both regions have a lower than average stellar mass fraction and therefore additional embedded young stars would bring them closer to the average. However, the data argue against a significant population of embedded sources. First, because the peaks in the Σ_{dust} map do correspond to local peaks in the *HST* detected Σ_{\star} map. Secondly, because there are no corresponding peaks in the MIPS 24 μm maps at these locations, while an embedded cluster would produce 24 μm emission. This emission would be detectable unimpeded by line-of-sight extinction. Finally, these regions have low observed dust temperatures, while embedded heating sources would increase their temperature.

6.2 Variations in gas-to-dust mass-ratio

If there are significant and systematic variation in r_{gd} , the conversion from Σ_{dust} to Σ_{gas} would be affected. Specifically, if the dust in the central part has been mostly destroyed, we would grossly underestimate the Σ_{gas} there, which would bring these points closer to the general trend (to the right in Fig. 8). The SED modelling shows that these regions are extremely depleted in PAHs. Is it plausible that the dust has also been destroyed? The increase required in the assumed value of r_{gd} for the central region of NGC 346 in order to make the variations in $frac_{M\star}$ disappear is a factor of 10 (r_{gd} equal to 12 500 instead of 1250).

An argument against significant dust destruction (or more generally significant variations in r_{gd}) is the very similar behaviour of H α and TIR (and 24 μm) emission. The rms of $\Sigma_{\text{TIR}}/\Sigma_{\text{H}\alpha}$ of the 115 pixels across the whole region is only 20 per cent and its behaviour is not spatially correlated with the stellar density or the radiation field density. This similar behaviour is also reflected in Fig. 5¹⁰. For the relatively low extinction conditions in NGC 346,

¹⁰ The scatter in $\Sigma_{\text{TIR}}/\Sigma_{\text{H}\alpha}$ of 20 per cent is much smaller than the scatter – about the mean trend in Fig. 5 – in the Σ_{TIR} and $\Sigma_{\text{H}\alpha}$, individually. This indicates that an above (below) average value of $\Sigma_{\text{H}\alpha}$ corresponds to an above (below) average value in Σ_{TIR} .

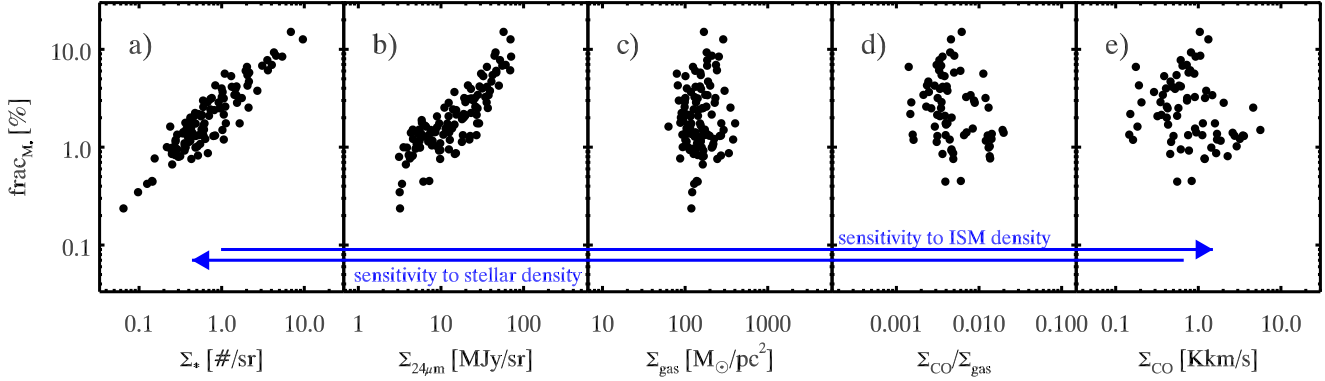


Figure 11. Scatter plots of the stellar mass fraction as a function of a number of key tracers. From left to right the tracer measures increasingly the ISM density and the presence of dense clumps. From right to left the sensitivity to the local stellar density increases. Σ_* is the surface density of the PMS+UMS stars. All panels span an identical dynamic range ($x_{\max}/x_{\min} = y_{\max}/y_{\min} = 1000$).

$\Sigma_{\text{H}\alpha}$ measures the chance for the starlight to be absorbed locally by the gas and Σ_{TIR} measures the same for the dust, the very similar behaviour (on scales of $6 \times 6 \text{ pc}^2$) of these tracers suggest a similar proportion of dust to gas across the region we studied. In case of very reduced dust abundances towards the central region, one would expect a limb-brightened shell in the dust emission, contrary to what is observed (Fig. 4a).

A relatively constant r_{gd} is further supported by the analysis of Lebouteiller et al. (2008) who measured the gas phase abundances along 13 different sight-lines across the NGC 346 complex. They find only minor variations in the gas phase abundances. Most importantly they find only 0.1dex variations in the S/H ratio while sulphur can be depleted into dust grains and strongly varying dust abundances would lead to variations of the abundance of sulphur remaining in the gas phase. We conclude that variations in r_{gd} that could explain the variations in $\text{frac}_{\text{M}\star}$ are improbable.

7 DISCUSSION

7.1 Effects of evolution

Our observations provide a snapshot of NGC 346 at one instance, roughly 3–5 Myr after the onset of the main star-formation event. During the star-formation epoch the amount of gas transformed into stars *must* evolve. Is the observed scatter in $\text{frac}_{\text{M}\star}$ caused by studying only this snapshot? In other words, is it possible that after the star formation has ceased, the $\text{frac}_{\text{M}\star}$ will be more homogeneous? Within the complex, different regimes can be discerned, as is illustrated in Fig. 12.

- *Region #1:* Main cluster with high dust surface densities and high number of stars. The region is detected in CO with moderate brightness.
- *Region #2:* Secondary cluster with fewer stars and less dust. Appears to be a ‘scaled-down’ version of the main cluster with bright H α and MIPS 24 μm emission and a moderately high $\text{frac}_{\text{M}\star}$.
- *Region #3:* This blob to the north-west of the complex has the highest dust surface density and low measured $\text{frac}_{\text{M}\star}$. It is detected in CO but the estimated molecular gas fraction is low.
- *Region #4:* The molecular ‘spur’ to the north-east has a small stellar mass fraction, high dust surface and no associated H α emission.

It is unlikely that these regions will all produce the same stellar mass fraction in the end. It can be argued that region #4, with its low current $\text{frac}_{\text{M}\star}$ but large reservoir of molecular gas, has the potential to still form a significant number of stars and thus boost its final mass fraction. However, the conditions in region #1–#3 do not seem to favour prominent continued star formation. Their ISM seems lacerated with ionized gas, as testified by the prominent H α emission and based on the CO map the molecular gas fraction is also low. We assess that, most likely, the observed differences between regions #1–#3 will persist.

7.2 Gas removal and stellar motions

We find a clear trend in stellar mass fraction from the central parts of NGC 346 to its outskirts. Within $\sim 15 \text{ pc}$ $\text{frac}_{\text{M}\star} \approx 10$ per cent while between 15–50 pc it is ~ 2 per cent. These zones are dominated by the cluster and the dispersed young stellar population, respectively as shown with the auto-correlation analysis of the stellar distribution (Gouliermis, Hony & Klessen 2014). The observed decrease of $\text{frac}_{\text{M}\star}$ with distance from the cluster is a signpost of lower SFE on the periphery (dispersed SF) than in the densest central parts (clustered SF). However, there are two caveats to consider, both related to the relative displacement of the stars and the ISM after birth.

A naive explanation for the present day systematic behaviour of the stellar mass fraction is the accumulation of stars, born in the periphery, in the central cluster. If such a process was possible, it would boost the observed $\text{frac}_{\text{M}\star}$ in the cluster while reducing its value outside. However this is an implausible scenario. Consider the free-fall time (τ_{ff}) of a star born in the periphery to be pulled into the cluster by gravity:

$$\tau_{\text{ff}} = \frac{\pi}{2} \frac{d^{3/2}}{\sqrt{GM_{\text{cl}}}}, \quad (2)$$

where d is the distance from the cluster, M_{cl} is the mass of the cluster (gas plus stars) and G is the gravitational constant. τ_{ff} is the *shortest* time-scale for a star to migrate towards the cluster, ignoring friction, virial velocities, rotational motions and the existence of any matter outside of the cluster that will exercise gravitational pull. For the observed M_{cl} of $\sim 10^5 M_{\odot}$ ($= N_{\star < 15 \text{ pc}} M_{\text{cat}} \text{frac}_{\text{M}\star}^{-1} = 2300 \cdot 4.3/0.1$) and a distance of 30 pc (the distance between region #1 and #3 in Fig. 12), $\tau_{\text{ff}} \approx 9 \text{ Myr}$, considerably longer than the ages of the PMS stars.

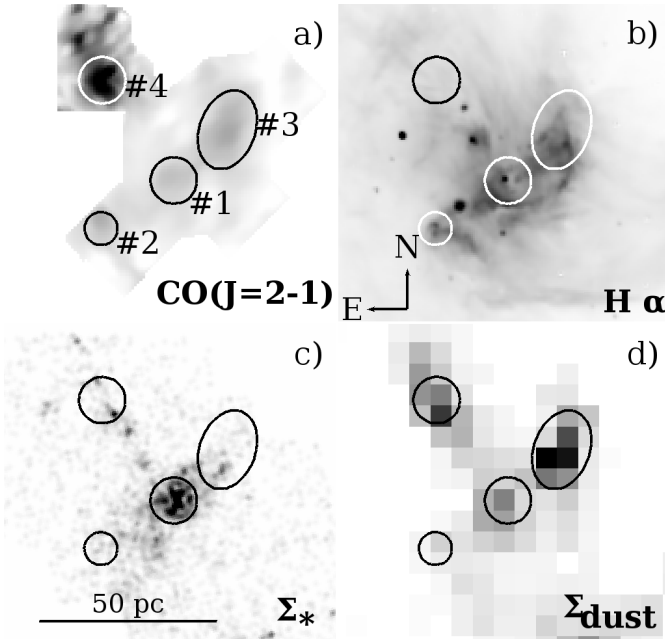


Figure 12. Distinct regions within the NGC 346 complex as observed in a number of key tracers: CO(J=2-1) integrate intensity map (Rubio et al. 2000, panel a), H α emission (Smith, Leiton & Pizarro 2000, panel b), young star density map based on Gouliermis et al. (2006, panel c) and the dust surface density (this work, panel d). All maps are shown in linear scale. We indicate four regions corresponding to local maxima in CO emission.

The second effect that could alter the observed $frac_{M\star}$ over time, is gas removal from the central region. When a cluster is formed, the gas left over from the star formation process may be rapidly removed by stellar winds (Lada, Margulis & Dearborn 1984). More recent work, however, suggests that the winds (and later, supernovae) may escape through low density channels formed in a hierarchical ISM (e.g. Rogers & Pittard 2013; Dale et al. 2014) causing much of the residual gas to remain. This seems to be the case for NGC 346. *HST* images of NGC 346 in the light of H α show the presence of residual gas. Molecular gas also appears to be present in the centre of the cluster despite the proximity of O stars (Fig. 12). *Chandra* observations reveal a low diffuse X-ray flux (Nazé et al. 2002), which indicates either that a supernova explosion has yet to occur, or the hot gas has escaped the region. Therefore gas expulsion cannot have produced the position dependence of $frac_{M\star}$. In further support of this conclusion are the findings of Smith (2012) and Smith et al. (in prep). These authors present high spectral resolution observations of H α and [O III] to examine the ionized gas motions in NGC 346. They find that the gas is quiescent. Data over ten slit positions covering the ionized nebula show no evidence for velocity splitting, even at the centre of the cluster. These results indicate that the gas is not being expelled by stellar winds but rather the dominant form of interaction is via stellar radiation to produce a classical expanding H II region.

An additional argument against the importance of efficient gas removal leading to a cavity in the central part of our map comes from the *Spitzer* detected embedded YSO candidates (Simon et al. 2007; Sewilo et al. 2013). These sources are young ($\lesssim 1$ Myr) and several of them are detected towards the central cluster. The number of detected YSO candidates towards the centre of NGC 346 is probably a lower limit, set by the difficulty of detecting individual point-sources which exhibit a mid-IR excess in the crowded clus-

ter region against the strong extended emission component due to the hot dust. The SFR derived from these objects ($> 3.2 \cdot 10^{-3} M_{\odot} \text{ yr}^{-1}$, Simon et al. 2007) is fully compatible with the average SFR for the entire 5 Myr event. If the clearing of the natal gas had taken place, one would expect to find few of these very young sources towards the central part of our map and probably also a diminishing trend of the star formation rate.

We conclude that the difference of a factor of ~ 5 in observed $frac_{M\star}$, most likely reflects a real difference in the average SFE in the clustered versus the dispersed star-forming regimes. This finding is consistent with theoretical models that assume that the star-formation efficiency is proportional to the free-fall time, hence denser regions have higher efficiencies (e.g. Elmegreen 2000; Krumholz & Tan 2007; Kruijssen 2012; Hopkins 2013).

7.3 High SFE – linked to low metallicity?

The SFE of NGC 346 is high even after averaging over ~ 150 pc (radius) scales (Fig. 7). As discussed in Kruijssen & Longmore (2014), this may be explained by the bias introduced by having chosen an active star forming complex as the object of study. These authors predict an offset of a factor of ~ 3 for the size of the regions we study, similar to what is observed. Additionally, this high value may be related to an above average star-formation efficiency in the clustered environment which dominates NGC 346. Nevertheless, it is still interesting to discuss the possible role of the lower metallicity for the following reasons. *i)* Kennicutt (2008) shows that low-metallicity galaxies like the SMC, as a whole, lie a bit (factor of ~ 3) above the general SK-relation. *ii)* The largest radius we measured is 150 pc. It is not obvious that by averaging to a larger distance, the derived SFE will decrease significantly – as it is also not obvious that it will stay high – because the next prominent star-forming complex (LHA 120-N76) is only about 300 pc projected distance away from NGC 346.

Because the SFE within individual star-forming clouds is a critical parameter for theories of galaxy evolution and galactic-scale star formation, with observable consequences on for example the galaxy luminosity function, there are many recent studies that have tried to assess whether the conversion of gas to stars depends on local ISM conditions and/or global galaxy parameters. Sain tonge et al. (2011) investigated the global gas content and star formation rates in ~ 200 galaxies in the redshift range between 0.025 and 0.05, finding a clear decrease in the star formation efficiency with increasing stellar mass. Resolved studies of nearby galaxies, meanwhile, have shown that the star formation efficiency on $\sim \text{kpc}$ scales varies with several ISM and Galactic-scale parameters, including stellar mass, dust-to-gas ratio, rotation velocity, orbital time and Hubble type (e.g. Leroy et al. 2013).

While the influence of any one parameter is difficult to isolate, a general conclusion that can be drawn from these studies is that low mass, low metallicity, late-type galaxies appear to be more efficient at forming stars from their molecular reservoir than high mass, metal-rich, early-type disc-galaxies. This could be in part a direct effect of metallicity: Dib (2011) show that low metallicity star forming regions may lie above the SK-relation for normal metallicity galaxies by a factor of 0.3dex as a consequence of higher SFE caused by less effective removal of the gas from the star forming region by stellar winds at low metallicity (Dib et al. 2011). The observed trend may also be due to an increasing fraction of molecular material located outside bound star-forming structures as the stellar mass and hence ISM pressure increases, although other effects are likely to contribute to the observed trends.

Our results in Sect. 5.1 are consistent with the picture emerging from lower resolution studies that molecular gas in low-metallicity, low-mass systems is somewhat more efficient at forming stars. In our case, we find that the mass of young stars in NGC 346 is high relative to its gas content, even after we average our measurements over scales that approach the spatial resolution of nearby galaxy surveys. However, we caution the reader to realise that the presented analysis of NGC 346 alone does not allow us to derive the global SMC star-formation efficiency nor conclude that it is above average.

8 SUMMARY

We present a detailed comparison of the surface density of young (PMS+UMS) stars (Σ_*) and dust surface density (Σ_{dust}) across the face of the most prominent star forming complex NGC 346 (N66) in the SMC. Σ_* is derived from individual stars identified in the colour-magnitude diagram based on *HST* photometry. Σ_{dust} is obtained via radiative transfer modeling of the infrared to submm spectral energy distribution. We measure these quantities in 115 independent pixels of $6 \times 6 \text{ pc}^2$ out to distances of $\sim 50 \text{ pc}$ from the main cluster, covering an area of $>4000 \text{ pc}^2$.

We find a correlation between Σ_* as a function of Σ_{dust} with a considerable scatter. A power law fit to the data yields a steep relation with an exponent of 2.6 ± 0.2 . We find that sight-lines towards the central $\lesssim 15 \text{ pc}$ exhibit *systematically* high values of $\Sigma_*/\Sigma_{\text{dust}}$ by a factor of ~ 5 compared to the rest of the complex.

We convert Σ_* to average star formation rate (SFR) surface densities (Σ_{SFR} in $\text{M}_\odot \text{ yr}^{-1} \text{ pc}^{-2}$) using 1) the observed mass function to derive the total stellar mass formed and 2) the time span over which these young stars have formed (5 Myr). This Σ_{SFR} is much less biased to the contribution of high-mass stars than luminosity based SFR tracers. The derived total SFR ($4 \pm 1 \cdot 10^{-3} \text{ M}_\odot \text{ yr}^{-1}$) is consistent (within 10 per cent) with Σ_{SFR} estimated from the extinction corrected $\text{H}\alpha$ emission integrated over the entire $\text{H}\alpha$ nebula.

On small scales ($6 \times 6 \text{ pc}^2$) the SFR estimated from indirect tracers (ionized gas or dust emission) compares very poorly with the SFR based on star counts. Across most of the studied region, $\text{H}\alpha$ systematically underestimates the local SFR, reaching a factor of 10 discrepancy in the central part of the complex. This discrepancy is due to ionizing photons escaping the local volume where the young stars are counted.

We convert Σ_{dust} to gas surface density (Σ_{gas}) using a constant gas-to-dust mass ratio ($r_{\text{gd}} = 1250$). This value is calibrated on our dust SED fitting method to yield the measured gas mass (from HI and CO) on a large scale, within a 500 arcsec radius centred on NGC 346. On this scale most of the gas mass is contained in the atomic phase and the influence the uncertain conversion factor from CO intensity to H_2 column density is small.

Using the derived Σ_{gas} and Σ_{SFR} , we place the pixels on a Schmidt-Kennicutt (SK) diagram. We find that individual pixels fall systematically above the SK-relation for integrated disc-galaxies by on average a factor of ~ 7 . This offset decreases as larger beams are used, consistent with the prediction from Kruijssen & Longmore (2014).

The observed offset is reminiscent of the results of Heiderman et al. (2010) and Wu et al. (2010) who show that the measured SFR lies above the galaxy averages when ‘zooming-in’ to parsec-scale on star forming clumps in the Milky Way. This is probably caused by less dense gas, which is inefficient in forming

stars, that is included in the galaxy-scale averages but not included when ‘zooming-in’ on individual clumps. A main difference with our analysis is that, even though we analyse $6 \times 6 \text{ pc}^2$ sized regions, we cover the full star-forming complex and find that the entire active region ($\sim 50 \text{ pc}$) lies consistently above the relation. In other words for NGC 346 one needs to ‘zoom-out’ beyond 50 pc to probe this less dense, non-star forming gas. The average over a larger area (90 pc radius) lies closer to the SK-relation but remains high by a factor of ~ 3 .

We present a map of the observed stellar mass fraction ($\text{frac}_{\text{M}_*} = \Sigma_* (\Sigma_{\text{gas}} + \Sigma_*)^{-1}$). frac_{M_*} is systematically high (~ 10 per cent) within the central 15 pc of the complex and systematically lower outside (2 per cent). We interpret this difference as the results of a higher star formation efficiency in the central zone. The inner 15 pc is dominated by young stars belonging to a centrally condensed cluster, while the outer parts are dominated by a dispersed population (Gouliermis, Hony & Klessen 2014). Therefore, the observed behaviour could reflect a change in star-formation efficiency between clustered and non-clustered star-formation.

ACKNOWLEDGEMENTS

Herschel is an ESA space observatory with science instruments provided by European-led Principal Investigator consortia and with important participation from NASA. Based in part on observations made with the NASA/ESA Hubble Space Telescope, obtained from the data archive at the Space Telescope Science Institute (STScI). STScI is operated by the Association of Universities for Research in Astronomy, Inc. under NASA contract NAS 5-26555. This work is based in part on observations made with the Spitzer Space Telescope, which is operated by the Jet Propulsion Laboratory, California Institute of Technology under a contract with NASA. This publication is based in part on data acquired with the Atacama Pathfinder Experiment (APEX). APEX is a collaboration between the Max-Planck-Institut für Radioastronomie, the European Southern Observatory, and the Onsala Space Observatory. We thank Sean Points and Roger Leighton for kindly making available the MCELS $\text{H}\alpha$ data. SH and RSK acknowledge support from the *Deutsche Forschungsgemeinschaft* (DFG) in the collaborative research project SFB881 The Milky Way System (subprojects B1, B2, and B5) as well as in the priority program SPP 1573 Physics of the Interstellar Medium. RSK furthermore acknowledges support from the European Research Council under the European Community's Seventh Framework Programme (FP7/2007-2013) via the ERC Advanced Grant STARLIGHT (project number 339177). DAG kindly acknowledges financial support by the German Research Foundation through grant GO 1659/3-1. SD is supported by a Marie-Curie Intra European Fellowship under the European Community's Seventh Framework Program FP7/2007-2013 grant agreement no 627008 AH acknowledges support from the Centre National d'Etudes Spatiales (CNES) and funding from the Deutsche Forschungsgemeinschaft (DFG) via grants SCHI 536/5-1 and SCHI 536/7-1 as part of the priority program SPP 1573 'ISM-SPP: Physics of the Interstellar Medium'. MYL acknowledges supports from the DIM ACAV of the Region Ile de France.

References

- Bernard J.-P. et al., 2008, *AJ*, 136, 919
- Bolatto A. D., Wolfire M., Leroy A. K., 2013, *ARA&A*, 51, 207
- Bonanos A. Z. et al., 2010, *AJ*, 140, 416
- Calzetti D. et al., 2007, *ApJ*, 666, 870
- Chen C.-H. R. et al., 2010, *ApJ*, 721, 1206

- Chen C.-H. R. et al., 2014, *ApJ*, 785, 162
- Cignoni M., Tosi M., Sabbi E., Nota A., Gallagher J. S., 2011, *AJ*, 141, 31
- Clark P. C., Glover S. C. O., 2014, *MNRAS*, 444, 2396
- Dale D. A., Helou G., Contursi A., Silbermann N. A., Kolhatkar S., 2001, *ApJ*, 549, 215
- Dale J. E., Ngoumou J., Ercolano B., Bonnell I. A., 2014, *MNRAS*, 442, 694
- Dib S., 2011, *ApJ*, 737, L20
- Dib S., Piau L., Mohanty S., Braine J., 2011, *MNRAS*, 415, 3439
- Dickel J. R., Gruendl R. A., McIntyre V. J., Amy S. W., 2010, *AJ*, 140, 1511
- Draine B. T., Li A., 2007, *ApJ*, 657, 810
- Elmegreen B. G., 2000, *ApJ*, 530, 277
- Evans, II N. J. et al., 2009, *ApJS*, 181, 321
- Galametz M. et al., 2013, *MNRAS*, 431, 1596
- Galliano F. et al., 2011a, *A&A*, 536, A88
- Galliano F. et al., 2011b, *A&A*, 536, A88
- Goodman A. A., 2004, in *Astronomical Society of the Pacific Conference Series*, Vol. 323, *Star Formation in the Interstellar Medium: In Honor of David Hollenbach*, Johnstone D., Adams F. C., Lin D. N. C., Neufeld D. A., Ostriker E. C., eds., p. 171
- Gordon K. D. et al., 2011, *AJ*, 142, 102
- Gordon K. D. et al., 2014, *ApJ*, 797, 85
- Gouliermis D. A., 2012, *Space Sci. Rev.*, 169, 1
- Gouliermis D. A., Dolphin A. E., Brandner W., Henning T., 2006, *ApJS*, 166, 549
- Gouliermis D. A., Hony S., Klessen R. S., 2014, *MNRAS*, 439, 3775
- Gutermuth R. A., Pipher J. L., Megeath S. T., Myers P. C., Allen L. E., Allen T. S., 2011, *ApJ*, 739, 84
- Hao C.-N., Kennicutt R. C., Johnson B. D., Calzetti D., Dale D. A., Moustakas J., 2011, *ApJ*, 741, 124
- Harries T. J., Hilditch R. W., Howarth I. D., 2003, *MNRAS*, 339, 157
- Haser S. M., Pauldrach A. W. A., Lennon D. J., Kudritzki R.-P., Lennon M., Puls J., Voels S. A., 1998, *A&A*, 330, 285
- Heiderman A., Evans, II N. J., Allen L. E., Huard T., Heyer M., 2010, *ApJ*, 723, 1019
- Hony S. et al., 2010, *A&A*, 518, L76
- Hopkins P. F., 2013, *MNRAS*, 428, 1950
- Indebetouw R. et al., 2008, *AJ*, 136, 1442
- Israel F. P., Maloney P. R., 2011, *A&A*, 531, A19
- Jeffries R. D., 2012, *Are There Age Spreads in Star Forming Regions?*, Moitinho A., Alves J., eds., p. 163
- Kennicutt R. C., Evans N. J., 2012, *ARA&A*, 50, 531
- Kennicutt, Jr. R. C., 2008, in *Astronomical Society of the Pacific Conference Series*, Vol. 390, *Pathways Through an Eclectic Universe*, Knapen J. H., Mahoney T. J., Vazdekis A., eds., p. 149
- Kim S., Staveley-Smith L., Dopita M. A., Sault R. J., Freeman K. C., Lee Y., Chu Y.-H., 2003, *ApJS*, 148, 473
- Kiseleva L. G., Colin J., Dauphole B., Eggleton P., 1998, *MNRAS*, 301, 759
- Kroupa P., 2001, *MNRAS*, 322, 231
- Kruijssen J. M. D., 2012, *MNRAS*, 426, 3008
- Kruijssen J. M. D., Longmore S. N., 2014, *MNRAS*, 439, 3239
- Krumholz M. R., Tan J. C., 2007, *ApJ*, 654, 304
- Lada C. J., Lombardi M., Alves J. F., 2010, *ApJ*, 724, 687
- Lada C. J., Margulis M., Dearborn D., 1984, *ApJ*, 285, 141
- Lebouteiller V., Bernard-Salas J., Brandl B., Whelan D. G., Wu Y., Charmandaris V., Devost D., Houck J. R., 2008, *ApJ*, 680, 398
- Leroy A. K. et al., 2013, *AJ*, 146, 19
- Li Y. et al., 2013, *ApJ*, 768, 180
- Longmore S. N. et al., 2013, *MNRAS*, 429, 987
- Markwardt C. B., 2009, in *Astronomical Society of the Pacific Conference Series*, Vol. 411, *Astronomical Data Analysis Software and Systems XVIII*, Bohlender D. A., Durand D., Dowler P., eds., p. 251
- Massey P., Parker J. W., Garmany C. D., 1989, *AJ*, 98, 1305
- Mathis J. S., Mezger P. G., Panagia N., 1983, *A&A*, 128, 212
- Mauch T., Murphy T., Buttery H. J., Curran J., Hunstead R. W., Piestrzynski B., Robertson J. G., Sadler E. M., 2003, *MNRAS*, 342, 1117
- Meixner M. et al., 2013, *AJ*, 146, 62
- Mokiem M. R. et al., 2006, *A&A*, 456, 1131
- Murphy E. J. et al., 2011, *ApJ*, 737, 67
- Nazé Y., Hartwell J. M., Stevens I. R., Corcoran M. F., Chu Y.-H., Koenigsberger G., Moffat A. F. J., Niemela V. S., 2002, *ApJ*, 580, 225
- Nota A. et al., 2006, *ApJ*, 640, L29
- Onodera S. et al., 2010, *ApJ*, 722, L127
- Planck Collaboration et al., 2011, *A&A*, 536, A17
- Preibisch T., 2012, *Research in Astronomy and Astrophysics*, 12, 1
- Rathborne J. M. et al., 2014, *ApJ*, 786, 140
- Reid W. A., Payne J. L., Filipović M. D., Danforth C. W., Jones P. A., White G. L., Staveley-Smith L., 2006, *MNRAS*, 367, 1379
- Relaño M., Kennicutt, Jr. R. C., Eldridge J. J., Lee J. C., Verley S., 2012, *MNRAS*, 423, 2933
- Rieke G. H., Alonso-Herrero A., Weiner B. J., Pérez-González P. G., Blaylock M., Donley J. L., Marcillac D., 2009, *ApJ*, 692, 556
- Rogers H., Pittard J. M., 2013, *MNRAS*, 431, 1337
- Rubio M., Contursi A., Lequeux J., Probst R., Barbá R., Boulanger F., Cesarsky D., Maoli R., 2000, *A&A*, 359, 1139
- Sabbi E. et al., 2008, *AJ*, 135, 173
- Saintonge A. et al., 2011, *MNRAS*, 415, 61
- Sandstrom K. M., Bolatto A. D., Draine B. T., Bot C., Stanimirović S., 2010, *ApJ*, 715, 701
- Sauvage M., Vigroux L., Thuan T. X., 1990, *A&A*, 237, 296
- Scalo J. M., 1986, *Fund. Cosmic Phys.*, 11, 1
- Schuller F., Nord M., Vlahakis C., Albrecht M., Beelen A., Bertoldi F., Müller S., Schaaf R., 2010, *BoA - The Bolometer Data Analysis Software: User and Reference Manual*, 4th edn. ESO
- Sewilo M. et al., 2013, *ApJ*, 778, 15
- Simon J. D. et al., 2007, *ApJ*, 669, 327
- Smith C., Leiton R., Pizarro S., 2000, in *Astronomical Society of the Pacific Conference Series*, Vol. 221, *Stars, Gas and Dust in Galaxies: Exploring the Links*, Alloin D., Olsen K., Galaz G., eds., p. 83
- Smith L. J., 2012, in *Astronomical Society of the Pacific Conference Series*, Vol. 465, *Proceedings of a Scientific Meeting in Honor of Anthony F. J. Moffat*, Drissen L., Rubert C., St-Louis N., Moffat A. F. J., eds., p. 416
- Vutisalchavakul N., Evans, II N. J., 2013, *ApJ*, 765, 129
- Williams M. J., Bureau M., Cappellari M., 2010, *MNRAS*, 409, 1330
- Wu J., Evans, II N. J., Shirley Y. L., Knez C., 2010, *ApJS*, 188, 313
- Zubko V., Dwek E., Arendt R. G., 2004, *ApJS*, 152, 211
- Zubko V. G., Mennella V., Colangeli L., Bussolotti E., 1996, *MNRAS*, 282, 1321